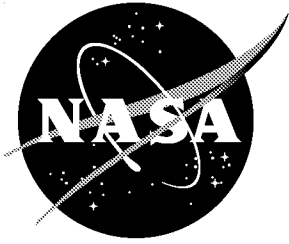


NASA/TP-2002-211779



Turbulent Navier-Stokes Flow Analysis of an Advanced Semispan Diamond-Wing Model in Tunnel and Free Air at High-Lift Conditions

*Farhad Ghaffari, Robert T. Biedron, and James M. Luckring
Langley Research Center, Hampton, Virginia*

August 2002

The NASA STI Program Office ... in Profile

Since its founding, NASA has been dedicated to the advancement of aeronautics and space science. The NASA Scientific and Technical Information (STI) Program Office plays a key part in helping NASA maintain this important role.

The NASA STI Program Office is operated by Langley Research Center, the lead center for NASA's scientific and technical information. The NASA STI Program Office provides access to the NASA STI Database, the largest collection of aeronautical and space science STI in the world. The Program Office is also NASA's institutional mechanism for disseminating the results of its research and development activities. These results are published by NASA in the NASA STI Report Series, which includes the following report types:

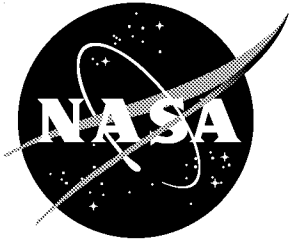
- TECHNICAL PUBLICATION. Reports of completed research or a major significant phase of research that present the results of NASA programs and include extensive data or theoretical analysis. Includes compilations of significant scientific and technical data and information deemed to be of continuing reference value. NASA counterpart of peer-reviewed formal professional papers, but having less stringent limitations on manuscript length and extent of graphic presentations.
- TECHNICAL MEMORANDUM. Scientific and technical findings that are preliminary or of specialized interest, e.g., quick release reports, working papers, and bibliographies that contain minimal annotation. Does not contain extensive analysis.
- CONTRACTOR REPORT. Scientific and technical findings by NASA-sponsored contractors and grantees.
- CONFERENCE PUBLICATION. Collected papers from scientific and technical conferences, symposia, seminars, or other meetings sponsored or co-sponsored by NASA.
- SPECIAL PUBLICATION. Scientific, technical, or historical information from NASA programs, projects, and missions, often concerned with subjects having substantial public interest.
- TECHNICAL TRANSLATION. English-language translations of foreign scientific and technical material pertinent to NASA's mission.

Specialized services that complement the STI Program Office's diverse offerings include creating custom thesauri, building customized databases, organizing and publishing research results ... even providing videos.

For more information about the NASA STI Program Office, see the following:

- Access the NASA STI Program Home Page at <http://www.sti.nasa.gov>
- E-mail your question via the Internet to help@sti.nasa.gov
- Fax your question to the NASA STI Help Desk at (301) 621-0134
- Phone the NASA STI Help Desk at (301) 621-0390
- Write to:
NASA STI Help Desk
NASA Center for AeroSpace Information
7121 Standard Drive
Hanover, MD 21076-1320

NASA/TP-2002-211779



Turbulent Navier-Stokes Flow Analysis of an Advanced Semispan Diamond-Wing Model in Tunnel and Free Air at High-Lift Conditions

*Farhad Ghaffari, Robert T. Biedron, and James M. Luckring
Langley Research Center, Hampton, Virginia*

National Aeronautics and
Space Administration

Langley Research Center
Hampton, Virginia 23681-2199

August 2002

Available from:

NASA Center for AeroSpace Information (CASI)
7121 Standard Drive
Hanover, MD 21076-1320
(301) 621-0390

National Technical Information Service (NTIS)
5285 Port Royal Road
Springfield, VA 22161-2171
(703) 605-6000

Summary

Turbulent Navier-Stokes computational results are presented for an advanced diamond wing semispan model at low-speed, high-lift conditions. Turbulence effects are accounted for by utilizing the Spalart-Allmaras model. The numerical results are obtained in support of a wind-tunnel test that was conducted in the National Transonic Facility at the NASA Langley Research Center. The model incorporated a generic fuselage and was mounted on the tunnel sidewall using a constant-width non-metric standoff. The objectives of the numerical study were in several parts. They included the numerical simulation of the NTF empty tunnel flow characteristics, semispan high-lift model with the standoff in the tunnel environment, semispan high-lift model with the standoff in free-air, and semispan high-lift model without the standoff in free-air. The computations were performed at flow conditions of $\alpha=10^\circ$, $M_\infty=0.2$, and $Re_c=24.2 \times 10^6$ which corresponded to a nominal approach and landing situation. An approach was developed for the numerical simulation of the empty-tunnel sidewall boundary-layer characteristics. The lessons learned from the approach were then applied to simulate the flow over the semispam model in the tunnel environment.

The computed high-lift flow characteristics for the model in both the tunnel and in free-air environment are presented. The computed wing pressure distributions agreed well with the measured data and they both indicated a small effect due to the tunnel wall interference effects. However, the wall interference effects were found to be relatively more pronounced in the measured and the computed lift, drag and pitching moment. Although the magnitudes of the computed forces and moment were slightly off compared to the measured data, the increments due the wall interference effects were predicted reasonably well. The numerical results are also presented on the combined effects of the tunnel sidewall boundary layer and the standoff geometry on the fuselage forebody pressure distributions and the resulting impact on the configuration longitudinal aerodynamic characteristics.

Introduction

The high-lift flow and the resulting aerodynamics experienced by an aircraft in take-off and landing are some of the most complex and difficult phenomenon to simulate, either experimentally with wind-tunnel tests, or numerically with the computational fluid dynamics (CFD) methods. For an aircraft to achieve the high-lift performance levels, required during takeoff and landing, it typically deploys mechanical systems that are referred to as high-lift devices. These devices are usually comprised

of leading and trailing edge flaps designed to maintain attached flow over the vehicle for acceptable aerodynamic efficiency and handling qualities at the elevated lift conditions. However, for high performance military aircraft (subject of the present study) this must be achieved within the context of a relatively thin, low aspect ratio wing, and thus the resultant high-lift flow field can vary considerably from that of conventional commercial transport configurations.

The numerical simulation of high-lift flows is very difficult because of the inherent geometrical complexity as well as some very complex flow

interactions that can occur. Such geometrical complexity introduced by high-lift devices includes physical gaps, cavity or cove regions, exposed flap side-edges that are often sharp, sharp or rounded flap hinge-lines, etc. These geometrical features can induce flow separation from either a smooth surface or a surface discontinuity that may roll up into a vortex flow, cause vortex breakdown, develop vortex boundary-layer interaction, produce confluent boundary-layers, result in unsteady flow and/or stalled flow, etc. These geometrical complexities and the resulting complex flow fields at high-lift conditions give rise to challenges that are difficult to address either experimentally or numerically. In addition to these challenges are the difficulties associated with transitional flow, aeroelastic effects, and tunnel wall interference effects particularly for semispan model testing.

Progress has been made in recent years to numerically simulate the complex high-lift flow aerodynamics with Reynolds-Averaged Navier-Stokes (RANS) formulations based on multiblock structured grid technology (refs. 1-3) with various degrees of success. However, the geometrical complexity of the high-lift configuration often requires a tremendous amount of time and resources to be spent in grid generation to set up such a computation. An alternative approach based on the unstructured grid technology has received attention in the recent years (refs. 4, 5), primarily because of its inherent flexibility in discretizing complex geometry. However, it is also widely believed that the existing unstructured grid technology, with capabilities to simulate the complex high-lift viscous flow characteristics, is still in the developmental stage and may not be ready for application by the general user community.

The overall CFD plan for the present numerical study, shown schematically in figure 1, consists of two primary objectives. The first objective is to validate a state-of-the-art RANS method for predicting the low-speed high-lift aerodynamics of an advanced high-performance military wing concept recently tested in the National Transonic Facility (NTF), (ref. 6), at the

NASA Langley Research Center (LaRC). The wind-tunnel model was designed as part of a multi-national collaborative effort (ref. 7) under the auspices of The Technical Cooperation Program (TTCP). The TTCP participants involved in this effort included the United States Department of Navy, National Aeronautics and Space Administration (NASA), and the United Kingdom Defense Evaluation and Research Agency (DERA). The wing had a diamond shaped planform incorporating a full span leading-edge flap, a part-span slotted trailing-edge flap, and a deflectable shroud ahead of the trailing-edge flap. The wing was mounted on a generic fuselage that was tested as a semispan configuration. The semispan model was mounted on the tunnel sidewall and included a 'non-metric standoff' designed to minimize the effect of the tunnel sidewall boundary layer on the configuration aerodynamics. The term non-metric refers to a component of a wind-tunnel model for which its contribution to the aerodynamic forces and moments are not measured by the model balance system. In addition to other objectives, the test was conducted primarily to assess high-lift rigging effects and to develop a database for CFD code validation. Data from this experiment include static surface pressures, configuration forces and moments, and aeroelastic deformations for many high-lift settings.

For the present code validation purposes, the CFD model included not only the semispan configuration but also a representation of the wind tunnel test section that was configured for solid wall testing (i.e., closed slots). The focus of the present numerical analysis is on a high-lift configuration with a specific rigging arrangement designed for approach and landing conditions. Referring to the schematic of the overall CFD plan shown in figure 1, these computations include an empty tunnel simulation to validate the viscous sidewall flow (fig. 1a) and then a simulation of the model-in-tunnel configuration (fig. 1b).

The second objective of this study is to numerically assess wind-tunnel wall interference effects for this configuration. This is

accomplished numerically through a systematic removal of wall interference effects due to solid-wall confinement (fig. 1c) and due to viscous sidewall interaction (fig. 1d). Experimental wall interference effects were also obtained (ref. 8), and these are used to help assess the numerical results. Previous semispan test technology at NTF has been developed for commercial transport configurations (refs. 9, 10) and the present effort complements this capability for this slender vehicle. The present computational results are all obtained with a multiblocked structured grid code known as CFL3D (ref. 11) coupled with the Spalart-Allmaras (SA) model (ref. 12) to account for turbulent flow effects.

Symbols

BC	boundary condition	M_∞	free-stream Mach number
BL	boundary layer	MIF	Model/standoff-In-Free-air
b/2	reference semispan, 2.6927 ft.	MIT	Model/standoff-In-Tunnel
C_D	drag coefficient, $\text{Drag}/q_\infty S_{\text{ref}}$	MNIF	Model/No-standoff-In-Free-air
C_L	lift coefficient, $\text{Lift}/q_\infty S_{\text{ref}}$	NASA	National Aeronautics and Space Administration
C_m	pitching moment coefficient, Pitching moment/ $q_\infty S_{\text{ref}} \bar{c}$	NTF	National Transonic Facility
C_p	pressure coefficient, $(p-p_\infty)/q_\infty$	OL	overlap
CFD	computational fluid dynamics	p	local static pressure, psf
C-O	grid topology, C streamwise and O circumferential	p_∞	free-stream static pressure, psf
c	cruise wing local chord, ft.	q_∞	free-stream dynamic pressure, psf
c_{ref}	cruise wing reference chord at $Y/(b/2)=0.3$, 3.295 ft.	RANS	Reynolds-Averaged Navier-Stokes
\bar{c}	wing mean aerodynamic chord, 3.143 ft.	R_{ft}	unit Reynolds number, per foot
DERA	Defense Evaluation and Research Agency	$R_{\bar{c}}$	Reynolds number, based on \bar{c}
FP	flat plate	S_{ref}	wing reference semi-area, 6.5908 ft ² .
H-H	grid topology, H streamwise and H spanwise	SA	Spalart-Allmaras
H-O	grid topology, H streamwise and O circumferential	TTCP	The Technical Cooperation Program
LaRC	Langley Research Center	TE	trailing edge
LE	leading edge	TEF	trailing-edge flap
LEF	leading-edge flap	TS	tunnel station
		u/U_∞	local/free-stream axial velocity ratio
		WIC	wall interference correction
		X/c	fraction of wing local chord
		$Y/(b/2)$	fraction of model semispan
		X,Y,Z	model reference coordinate system
		α	angle of attack, degrees
		α_c	corrected angle of attack due to wind tunnel wall interference effect, degrees
		u^+	inner law velocity, u/v^*
		v^*	wall friction velocity, $(\tau_w/\rho)^{1/2}$
		y^+	inner law distance, yv^*/ν
		μ	viscosity
		ν	kinematic viscosity, μ/ρ
		ρ	density
		τ_w	wall shear stress, $(\mu du/dy)_w$

Test Description and Preliminary Analysis

Model Description

The semispan wind-tunnel model consisted of a generic fuselage with a 1.5-inch non-metric constant-width standoff and a cropped diamond wing planform with leading and trailing edge sweeps of 40° , and -40° , respectively. The wing was designed for multi-mission interdisciplinary military requirements for cruise, high angle of attack maneuver, as well as for low-speed, high-lift performance. The photographs in figure 2 show the high-lift version of the model from two different perspective views.

The semispan model was 7.7 ft long and 2.7 ft wide excluding the 1.5-inch constant width non-metric standoff. Figure 3(a) shows the planform view of the model that was instrumented with approximately 450 orifices to measure the static surface pressures. The majority of the pressure orifices were distributed over the wing and in particular around the high-lift system. The wing pressure orifices were primarily distributed along six chord-wise stations located at $Y/(b/2)=0.15, 0.30, 0.45, 0.55, 0.70$, and 0.80 .

The baseline conditions for the high-lift wing model included a full span 22° deflected leading-edge flap (LEF), a partial span 23° deflected shroud, and a partial span 35° deflected trailing-edge flap (TEF). Figure 3(b) shows a typical wing high-lift sectional cut. All the flap component deflection angles are measured in a sectional chord plane and have constant chord dimensions. The gap and overlap (OL) dimensions for the slotted TEF of the high-lift model are referenced to the cruise wing (undeflected LEF, shroud, and TEF) chord (c) located at $Y/(b/2)=0.3$. The gap and OL for this baseline high-lift model were set at $0.5\%c_{ref}$ and $2\%c_{ref}$, respectively.

A downstream view of the model (with cruise wing configuration) mounted on the NTF tunnel sidewall is shown in figure 4(a), whereas the photograph in figure 4(b) illustrates a close-up

view of the deployed high-lift components. The model angle of attack rotation was accommodated by the use of the pitch turntable, which was inserted into the tunnel sidewall and connected to a 5-component semispan balance to measure the forces and moments acting on the model. The standoff geometry component was not included in the balance overall forces and moments measurement. (i.e., non-metric). The measured data was subsequently corrected for the blockage effects and to exclude the contribution from the blunt base of the fuselage.

Test Matrix and the Configuration/Flow Conditions of Interest

The primary purpose of the test was to develop an experimental database for four different variations of the diamond wing with the emphasis on the high-lift aerodynamic performance for various flap-rigging arrangements (gap and overlap). These configuration variations, see Table 1, include two high-lift riggings for approach and landing, one high-lift rigging for take-off, and the baseline cruise-model with no control surface deflections. Each of the three high-lift configurations was tested with three combinations of gap (i.e., $0.5\%c_{ref}$, $1.5\%c_{ref}$, $2.5\%c_{ref}$) and overlap (i.e., $-1.0\%c_{ref}$, $0.5\%c_{ref}$, $1.5\%c_{ref}$, $2.0\%c_{ref}$, $3.0\%c_{ref}$) settings. In addition, some intermediate gap and overlap settings for the high-lift configurations along with a maneuver configuration with a hinged TEF were also included in the test.

Configuration	LEF	Shroud	TEF
High-lift, approach/landing	22°	23°	35°
High-lift, approach/landing	22°	17°	35°
High-lift, take-off	22°	0°	20°
Cruise	0°	0°	0°

Table 1. Configurations tested in the NTF.

Limited aerodynamic analysis of the experimental data has been performed and reported in reference 13. In this reference, the estimates for the data repeatability have been

reported, in terms of 2σ (σ denotes the standard deviation), for the normal force, axial force, and pitching moment coefficients to be within 0.00030, 0.00004 and 0.00014, respectively. Furthermore, similar estimates are also reported for the measured upper and lower surface pressure coefficients to be within 0.0046 and 0.0083, respectively. Although not used in the present numerical study, a technique was used as part of the NTF test to measure the aeroelastic deformation of the slotted-flaps on the model (ref. 14). In general, these deformations were found to be aerodynamically negligible.

The high-lift wing designed for approach and landing was chosen as the baseline configuration for the present numerical analysis. The planform view and the corresponding high-lift rigging for the selected baseline configuration were shown earlier in figure 3. Representative flow conditions for approach and landing were also selected for the numerical analysis and they are $\alpha=10^\circ$, $M_\infty=0.2$, and $R_\tau=24.2 \times 10^6$.

NTF Tunnel Description

The NTF is a fan driven, closed-circuit operational tunnel. The tunnel nominal test section is 25 feet long and has a square cross section with a side dimension of 8.202 feet (see figure 5). The four corners of the tunnel walls are filled symmetrically with right triangular fillets with the side dimensions (i.e., equilateral sides) of approximately 6 inches attached to the tunnel walls. It was learned that available geometry data for the upstream contraction cone and the settling chamber were not sufficient for use in CFD model simulation. As a result, the initial CFD analysis focused only on modeling the interior flow within the nominal NTF test section.

The NTF is primarily a transonic wind-tunnel facility designed to provide aerodynamic data on sub-scale models at high unit Reynolds numbers achieved through elevated pressures and cryogenic temperatures. The tunnel floor and the ceiling are each equipped with six longitudinal slots to accommodate testing at transonic speeds. However, the primary focus of the present

diamond wing test was to acquire aerodynamic data on high-lift configuration at lower speed regime (i.e., $0.2 < M_\infty < 0.5$).

The test was conducted with the tunnel slots closed in order to eliminate any effects due to interactions between the trailing wake and the slots; this is a common approach to high-lift testing. With this testing approach, a conventional solid wall interference correction (WIC) method can be used to account for the interference effects induced by the tunnel walls. The implementation of the WIC method in the NTF is described in reference 8. Two factors contributed to the testing of the model in the air mode. The first was because the model was not designed for cryogenic testing environment. The second factor was associated with the relatively large model size that was determined to produce the full-scale flight Reynolds number under elevated pressures.

NTF Empty Tunnel Flow Characterization Test

Prior to the diamond wing test, an effort was undertaken to characterize the flow in the NTF empty tunnel environment. As part of this flow characterization test (ref. 15), a rake system was employed to measure the BL profile on the tunnel sidewall where the semispan model was to be mounted (referred to as the model center of rotation). This model center of rotation is located at the tunnel station (TS) 13 ft, approximately half way between the tunnel floor and the ceiling (see figure 5). A schematic view of the BL rake is shown in figure 6(a). The rake was 6.25 inches tall and incorporated 29 probes. The first 8 probes were uniformly distributed over the first inch to measure the near wall pressure field.

A sample velocity profile derived from the measured pressure data at a nominal flow condition of $M_\infty=0.2$, $R_\tau=2 \times 10^6$ is shown in figure 6(b). Each experimental data point includes a horizontal band to indicate the corresponding fluctuation range of the measured quantity (ref. 15). At this flow condition, the measured velocity profile indicated that the edge of the boundary

layer (i.e., $u/U_\infty \sim 0.99$) occurs at a height of approximately 3.8 inches (96.52 mm). This data set is used to validate the numerical simulation of the empty tunnel sidewall boundary layer characteristics. Figure 6(b) also shows the model standoff superimposed on the empty tunnel BL profile for reference.

Turbulent Navier-Stokes Computations and Flow Field Analyses

Numerical Algorithm

The present numerical analysis is performed with the multiblock, structured-grid CFD code known as CFL3D (ref. 11). The code is well documented and has been extensively validated for variety of applications with different classes of flows and configurations (refs. 16-22). The algorithm is based on the compressible, time-dependent, Reynolds-Averaged Navier-Stokes (RANS) equations that are written in a curvilinear coordinate system. A cell-centered, finite volume approach is used to solve the equations in a conservative form. An upwind-biased, flux-difference-splitting scheme (ref. 23) is used to solve the inviscid terms whereas central differencing is applied to solve the viscous terms. Several turbulence models, from algebraic equation model to one and two equation models, have been incorporated in the code.

The present numerical results are all based on the one-equation model of Spalart-Allmaras (ref. 12). The solutions presented in this report are all obtained by the use of multi-gridding and mesh-sequencing techniques to accelerate the convergence characteristics. The various grid-block interfaces in the physical domain are patched to one another either in a two-dimensional planar form or a three-dimensional non-planar form. The flow primitive variables are interpolated across the various block interfaces using a searching technique based on a combination of linear and polynomial equations as discussed in reference 19.

NTF Empty Tunnel Numerical Flow Simulation

The empty tunnel flow simulation was conducted primarily for two reasons. The first reason was to establish that the tunnel sidewall BL could be reasonably simulated. The second reason was to determine whether a mixed viscous and inviscid boundary condition for modeling the tunnel walls was adequate to simulate the test section flow field.

The initial numerical model included only the nominal NTF test section and the tunnel sidewall was treated with a viscous boundary condition whereas the other three walls were simulated with an inviscid boundary condition. The characteristic inflow BC and outflow BC with specified pressure ratio (p/p_∞) of 1.0 were imposed at the tunnel inlet and exit plane. The tunnel corner fillets were not modeled in this study because their symmetric influence on the tunnel sidewall BL characteristics is expected to be small, particularly around the model center of rotation. Four sets of Cartesian grids (i.e., H-H topology) were generated with different grid resolutions ($0.5 < y^+ < 11.8$, y^+ is measured from the first cell center off the wall) to address grid sensitivity effects on the results. Pilot computations were performed at $M_\infty = 0.2$, and $R_{ft} = 2 \times 10^6$, based on the RANS formulation with Spalart-Allmaras (SA) turbulence model. As shown in figure 7, the correlation of these computed results (open symbols) with the measured BL thickness at TS 13 ft. (solid square) indicated a clear disagreement. This disagreement was rather expected because of the numerical model did not include a proper BL profile at the inflow plane (i.e., $X=0$).

Due to the simplicity of the tunnel sidewall BL characteristics, it was decided to explore the applicability of flat-plate (FP) theory:

$$\delta = 0.14(X)^{6/7}/(R)^{1/7} \quad (1)$$

for estimating the turbulent BL thickness growth along the tunnel sidewall. In this equation, X is measured from the flat plate LE and R is defined

as the Reynolds number per unit length (i.e., mm in this case). The flat-plate theory estimates of the BL thickness growth are also shown in figure 7 to be very close to the turbulent Navier-stokes results computed for the nominal NTF test section (buried under the RANS open symbol predictions). As a result, it was decided to use the flat-plate BL theory and the existing experimental data point (i.e., BL height of 3.8 inches (96.52 mm) at TS-13) to extrapolate a virtual origin to the NTF test section that would provide a better approximation of the BL thickness at TS-13. This analysis, as shown in figure 7, revealed the location of a virtual origin to be approximately 15 ft (4600 mm) ahead of the nominal NTF test section.

Finally the accuracy of the estimated NTF virtual origin by the flat-plate theory was varified by applying the turbulent (SA) Navier-Stokes method. This varification was performed by modifying a volume grid generated earlier for the computation of the nominal NTF test section (i.e., 65-axial, 129-normal to the sidewall, 65-lateral, $y^+ \sim 0.9$) to accommodate grids for the upstream extension of the tunnel geometry. The turbulent Navier-Stokes results for the boundary-layer height growth along the extended NTF sidewall is also shown (solid line) in figure 7. The Navier-Stokes results for the extended NTF sidewall clearly reaffirm that the flat-plate BL height estimates were very reasonable. It should be noted that with this approach the relatively complex contraction-cone and the settling-chamber geometry (unavailable for accurate numerical modeling) are essentially replaced with a simple linear upstream-extension of the square cross-section, tunnel geometry.

The measured velocity profile shown earlier in figure 6(b), is repeated in figure 8 along with the axial velocity profiles computed for the nominal (open symbols) and the extended NTF test section (solid line). The discrepancies between the measured data and the predictions with the nominal NTF test section are apparent. However, the comparison clearly illustrates an excellent agreement between BL rake measurements and the computed velocity profile with the extended

NTF test section.

The simulated boundary layer flow was also analyzed in terms of inner law variables, and the results are shown in figure 9(a). In this figure the computed CFD profile is compared with standard boundary layer theory for flat plate flow.

The theoretical results are given by:

$$\text{Laminar sublayer: } u^+ = y^+ \quad (2)$$

$$\text{Logarithmic layer: } u^+ = 1/\kappa \ln(y^+) + B \quad (3)$$

Spalding's law of the wall:

$$y^+ = u^+ +$$

$$e^{-\kappa B} [e^{-\kappa u^+} - 1 - \kappa u^+ - (\kappa u^+)^2/2 - (\kappa u^+)^3/6] \quad (4)$$

Law of the wake:

$$u^+ = 1/\kappa \ln(y^+) + B + 2 (\Pi/\kappa) \sin^2[(y/\delta) (\pi/2)] \quad (5)$$

In all cases $\kappa=0.4$ and $B=5.5$ which are standard values preferred by Spalding; for the wake flow $\Pi=0.7$ which is slightly high (but not unreasonable) when compared to Coles' recommended value of 0.55.

The CFD results are for the cell-center values, and the correlation between the CFD and the theoretical profiles is in general very good. The first cell center value occurs at a y^+ of about 0.4, and despite this resolution, there are only a few points fully within the laminar sublayer ($y^+ < 3.6$). It appears that a slightly less aggressive stretching would have been more appropriate for representing the inner-law profile as modeled by Spalding's law of the wall. Correlation between CFD and theory is very reasonable for the logarithmic layer ($100 < y^+ < 1000$) and degrades a little in the wake portion of the profile ($1000 < y^+$). Nonetheless, the predicted onset of the outer wake profile at approximately $y^+=2500$ is fairly well modeled by the law of the wake.

The inner-law analysis is useful for discerning the various flow physics regions of the turbulent

boundary layer associated with the presence of the wall. This analysis tends to compress the outer-law wake portion of the flow. To better observe this portion, the same profile is simply shown in primitive variables in figure 9(b). Here again the computed boundary layer from CFD follows the expected theoretical trends reasonably well. It should be noted that the onset of the wake-like profile ($y^+=2500$) corresponds approximately to $y/\delta=0.13$. Very little of the inner-law properties can be discerned in the conventional boundary-layer profile.

It should be noted that as part of the NTF empty-tunnel flow simulation study, though not presented here, turbulent (SA) Navier-Stokes computations were also carried out by simulating the viscous boundary-layer flow on all four walls of the extended tunnel geometry. The results from this study revealed that only a slight thinning of the sidewall BL occurred and that it did not manifest itself until reaching TS 5 ft. This thinning of the BL thickness was computed to be about 0.1 inch (less than 3 mm) at TS 13 ft. The empty tunnel flow simulation study demonstrated that the upstream extension and the grids employed were acceptable to simulate the sidewall BL characteristics. The extended NTF test section was used for all subsequent numerical simulations.

Model/standoff-In-Tunnel (MIT)

Numerical Grid Strategy: A multi-block structured grid was developed to discretize the semispan high-lift diamond wing model with the stand-off geometry in the nominal NTF test section (see figure 10). The semispan diamond wing numerical model is rotated and set at 10° angle-of-attack with respect to the tunnel free-stream. Provisions were made from the empty tunnel flow simulation to properly size the grid over the viscous sidewall and to accommodate the tunnel upstream block extension (not shown in figure 10). The volume grid consisted of 39-grid blocks and containing approximately 7 million grid points. No grid density study was performed on the diamond wing configuration. However, 7 million grid points has been shown, ref. 24, to be

sufficiently fine for predicting lift and drag to within 1% for a different configuration (i.e., wing-body-engine-nacelle transport model). Grid spacing for the model viscous surfaces were chosen to produce a y^+ of about 1 for the first cell center off the wall. In general, the overall grid topology can be grouped into five regions; 1) configuration forebody region with C-O grid, 2) fuselage top and bottom region with H-H grid, 3) aft-fuselage region with H-O grid, 4) fuselage standoff with H-H grid, and 5) the high-lift wing with C-O topology. The deflected wing trailing-edge flap was discretized with a C-H topology embedded within the main wing C-O grid. These grid blocks were patched with one another along common interfaces.

The XYZ-coordinate system for the grid is defined such that: positive X is from upstream to downstream, positive Y is normal to the sidewall, and positive Z is from tunnel ceiling to floor. The volume grid is defined in metric units where the viscous sidewall is located at $Y=-38.1$ mm (i.e., 1.5 inch standoff width) with the opposing side at $Y=2461.9$ mm. The overall longitudinal length of the nominal NTF test section is defined to be 7620 mm (i.e., 25 ft) long.

A close-up view of the surface grid for the semispan diamond wing model along with the tunnel sidewall grids is shown in figure 11. Surface grids are clustered in regions where the flow is expected to experience a rapid change such as acceleration or separation. These regions include the LEF and shroud hinge-lines, around the wing leading and trailing edges; TEF exposed side-edges, wing-fuselage junctures, etc. In addition, a stream-wise cut through the volume grid around the high-lift element is also shown in the right-hand side of the figure. The complexity of the geometry and the care taken to resolve the cove and the gap regions are clearly illustrated. The inboard edge of the deflected TE flap is abutted against the fuselage whereas on the outboard side a gap is created exposing to the side edges of the flap and the main wing element.

Loads associated with the fuselage blunt base flow are removed from the experimental

measurements and are expected to have a small induced effect on the wing. These loads are also removed from the numerical results, and thus it seemed unnecessary to model the detailed base flow physics (i.e., unsteady, turbulent viscous wake flows). Furthermore, such detailed modeling of the subject flow would also contribute to the complexity of the calculations and convergence difficulties. To mitigate such complications, an inviscid BC was used to model the blunt base of the fuselage. The grid topology for the fuselage base is an H-H that simply extends the associated grid on the fuselage blunt face longitudinally by stacking them downstream to the outflow plane. In addition, an H-H grid topology was used to abut against the exposed side edges of the TE flap (i.e., outboard side) and the exposed aft part of outboard wing-panel (i.e., inboard side). These grids were required to resolve the viscous flow on the subject side-edge panels.

Solution Development and Convergence Characteristics: Turbulent Navier-Stokes computations were performed by setting the tunnel free-stream conditions to $M_\infty=0.2$, $R_\infty=24.2 \times 10^6$, and at zero degree angle of attack. However, note that the geometric angle of attack (α) for the model is 10° , because as discussed previously, the numerical model is rotated to 10° angle of incidence relative to the tunnel free-stream condition. The computations were performed on the numerical aerodynamic simulation (NAS) Cray C-90 computer located at NASA Ames Research Center and required about 300 MW of memory. The flow solution, initiated from free-stream conditions, was advanced in time to a steady state, by using multi-grid, local time stepping, and mesh sequencing techniques to accelerate the convergence characteristics.

A solution development and convergence procedure was developed for this baseline MIT case that could be applied in a consistent way to the other cases in the present investigation. With this procedure, the overall solution convergence was achieved using mesh sequencing with three grid levels (i.e., coarse, medium, and fine). Figure 12(a) shows the overall solution convergence history that required about 60 hours of central

processing unit (cpu) time on a Cray C-90 with a single processor to achieve such characteristics. The coarse, medium, and fine grid solutions were converged over 4000, 3000, and 2000 iterations, respectively. Over the course of this solution development, the overall residuals were reduced by ~ 2.5 orders of magnitude and the oscillations in the computed total (i.e., summation of all viscous and inviscid surface boundaries) lift, drag, and pitching moment were reduced to a negligible level. Over the last 500 iterations of the fine grid solution, the variations in total lift, drag, and pitching moments were found to be approximately ± 0.0005 , ± 0.0002 , and ± 0.0005 , respectively. In addition, Table 2 presents the percent variation of forces and moment relative to the fine grid solution (at iteration 9000) for the coarse and medium grids at iterations 4000 and 7000, respectively.

Grid level	%C _L	%C _D	%C _M
Coarse	2.8	18.5	3.9
Medium	0.8	3.7	0.8

Table 2. Grid-level effects on computed longitudinal aerodynamic characteristics.

Figure 12(b) also shows a more quantitative variation of the residuals for each block during the course of the solution development at every 1000 iteration intervals. It should be noted that the largest oscillations in the block residuals are occurring in and around block 35 that is associated with the blunt fuselage base. These oscillations become fairly small over the fine grid solution development. The block residuals in the rest of the flow domain indicate a much better convergence rate than those associated with in and around block 35.

Computed Flow Field Analysis: General flow features computed over the model will be presented in this section, while the quantitative comparisons of the numerical prediction with experimental data will be discussed later. The computed flow features in terms of surface

pressure coefficients and streamlines for the MIT are shown in figure 13(a). The surface pressure coefficients are shown on the semispan diamond wing model, tunnel sidewall, inflow/outflow and the floor plane of the upstream portion of the extended NTF test section. The flow streamlines, shown in figure 13(a), correspond to the path of several particles released in the field near the tunnel sidewall just ahead of fuselage and around the leading edges of the wing and the trailing edge flap. In addition, a few particles were released close to the fuselage blunt base to highlight the associated wake flow-field structure. The particle traces are computed without any restriction to a particular computational grid plane.

The close up views of the computed flow characteristics over the model and the wing are shown in the left and right hand side of figure 13(b), respectively. The computed pressure coefficients along with the particle traces over the wing upper surface appear to indicate an attached flow on the deflected leading-edge flap, the expected flow expansion along the flap and the shroud hinge-lines, and a region of a fairly benign attached flow over the main wing panel. Figure 13(c) show a close up views of circulatory-trapped flow streamlines in the cove region (left hand-side image with the shroud geometry removed) and flow structures around the TEF side edge (right hand-side image). The computed results around the TEF indicate a region of low pressure that is associated with the vortical flow originating from the lower corner of the TEF side edge. This TEF side-edge flow separation forms a vortex that spills over to the flap upper surface. The close up views of the computed lower-surface pressure coefficients over the model and the TEF are shown in the right and left hand side images of figure 13(d), respectively. The results generally show flow compression at the nose of the fuselage and under the wing that is extended onto the neighboring fuselage. Also, note that the effect of the TEF side-edge vortex flow interaction with the outboard wing panel is evident by the presence of a low-pressure region on its aft lower surface as the flow accelerates through the gap. From a high-lift design standpoint, the computed flow characteristics indicate the desired attached

flow has successfully been maintained over the LEF, main wing, shroud, and TEF for most part of the inboard region at these conditions.

A stream-wise cut through the MIT numerical result, showing the overall view (top image) and the close-up view (bottom image) of the pressure field, at a longitudinal station of $Y=1.33$ ft (405 mm) is presented in figure 14. Relative to the model, this longitudinal cut is slightly inboard of the TEF side-edge that is at $Y=410$ mm. Similar to the earlier finding, the overall view of the pressure field indicate a trailing wake system that extends downstream to the tunnel outflow plane without getting close to the tunnel floor. The close-up view of the results generally shows the flow expansion over the LEF hinge line and over the TEF upper surface due the presence of the side-edge vortex flow.

A cross-flow cut through the MIT numerical result, showing the near field and the close up view of the pressure distribution around the geometry and the complex high-lift system, at $TS=2.74$ ft (835 mm) is presented in figure 15. This TS is 1.17 ft aft of the tunnel station 13 ft at which the model center-of-rotation is located (see figure 3(a)). The close-up view of the results clearly shows the presence of a vortex system on the TEF side-edge along with the flow expansion around the TEF leading edge and the resulting acceleration on its upper surface.

Model/Standoff-In-Free-air (MIF)

Numerical Grid Strategy: The grid strategy chosen for the MIF computations utilized the existing MIT grid without any alteration. The MIF grid required six new grid blocks to extend the MIT tunnel walls to the nominal far field (see figure 16). The radial extent of the far-field boundary was chosen to be about five overall fuselage body-lengths (i.e., $\sim 12.2\bar{C}$) away from the tunnel centerline.

These new blocks included two H-O topologies that wrapped around and patched to the NTF walls (one over the nominal test section and the other over the upstream extension part). The

remaining four H-H topologies were patched to the existing MIT standoff blocks that extended to the nominal far field boundary. These six blocks added a total of approximately 160,000 points to the existing MIT volume grid (i.e., 7 million grid points). Characteristic inflow/outflow boundary conditions are invoked on the exterior surfaces of the far-field boundary. Also, the plane-of-symmetry for this case is modeled as a viscous boundary similar to the MIT sidewall.

Computed Flow Field Analysis: Procedures identical to those developed to obtain the turbulent Navier-Stokes solutions for the MIT case were applied to acquire the computational results for the MIF case at the same flow conditions. The MIF solution development generated almost identical convergence characteristics as those of the MIT case shown earlier in figure 12. The computed pressure coefficients from the MIF solution is shown in figure 17 from two vantage points comparable to those shown earlier for the MIT results in figure 13. The surface pressures are mapped over the same contour range and the seeding locations for the particle traces are identical to those of the MIT with the exception of a few that are released near the configuration plane-of-symmetry in the new added blocks.

Qualitatively the computed streamlines and pressure coefficients appear to be very similar to those of the MIT results. Although it is difficult to discern from these figures, the detailed analysis indicated that the flow streamlines released near the plane-of-symmetry appear to maintain their curvature to a longer distance away from the configuration than those released in the MIT solution. This effect can be attributed to the confined flow field in the tunnel environment where the solid walls do not provide the same pressure relief as present in the MIF environment.

Model/No-standoff-In-Free-air (MNIF)

Grid strategy and results discussion: The volume-grid blocks associated with the standoff were extracted from the existing MIF computational grid. This modification resulted in

a total of 38 grid blocks, and ~6.5 million grid points, to remain for the numerical representation of the model/no-standoff in free-air (MNIF). The same boundary conditions as the MIF case were applied on all surfaces with the exception of the configuration plane-of-symmetry where the general symmetry plane boundary condition was imposed.

The computational procedure established under the MIT and MIF solution development were applied to obtain the turbulent Navier-Stokes solution for the MNIF case at $\alpha=10^\circ$, $M_\infty=0.2$, and $R_{\bar{c}}=24.2 \times 10^6$. Nearly identical solution convergence characteristics were achieved as those obtained for the earlier computations. The subsequent flow field analysis also indicated qualitatively very similar results for flow streamline traces and surface pressure contour mapping as those obtained from the MIT and MIF solutions and therefore not presented here. However, the quantitative results from MNIF solution will be correlated next with the experimental data, along with the results from the other CFD cases, that reveals considerable pressure differences around the fuselage forebody region.

Pressure, Force & Moment Predictions and Correlation with NTF Data

Two sets of experimental data, referred to as ‘with WIC’ and ‘without WIC’, will be presented in this report. While both data sets include all the standard wind-tunnel data corrections, the only difference between them is that one contains the solid-wall interference correction effect and the other does not. The application of WIC to correct the experimental data that corresponds to the flow conditions chosen for the numerical analysis resulted in an increase in the model angle of attack, free stream Mach number, and dynamic pressure. The corresponding increments to angle of attack (10°), free-stream Mach (0.2) and dynamic pressure (347.6 psf) were 0.6° , 0.001, and 4.54 psf, respectively. With the exception of the angle of attack, the increments to Mach number and dynamic pressure are considered relatively small in the present investigation. To

numerically complement the corrected experimental data, an additional MIF computation was performed at $M_\infty=0.2$, $R_\infty=24.2 \times 10^6$, and a higher free-stream angle-of-attack of 0.6° . As a result, the angle of attack for the numerical model (rotated to 10° angle of incidence relative to the tunnel free-stream flow) in this new computation is 10.6° which will be referred to as the corrected angle of attack (α_c). The results from this new MIF computation at $\alpha_c=10.6^\circ$, along with those originally planned will be correlated with the corresponding experimental data for surface pressure coefficients and overall forces and moment.

Surface Pressure Coefficients: The computed surface pressure coefficients, the NTF data for both with and without full corrections for wall interference effects, along with wing geometry sectional cuts are shown in figure 18. These pressure coefficients are shown at six chordwise stations on the wing, three over the inboard high-lift section (figure 18(a)), and three on the outboard panel (figure 18(b)). The experimental data for the three inboard stations are only shown for the wing main element because of some inconsistencies encountered in mapping the experimental pressure-orifice locations with the corresponding high-lift CFD model over the shroud and the TEF. Proper reference quantities, such as the shroud and TEF axis of rotation, were not available for consistent transformation of the CFD results to the experimental data or vice versa. Furthermore, the distributions of the experimental pressure orifices were also found to be slightly skewed with respect a constant span cut, particularly over the TEF component.

The CFD results are shown for four different cases that include the MIT, MIF, MNIF (all at $\alpha=10^\circ$), and the MIF at $\alpha_c=10.6^\circ$. The experimental data are shown for both corrected (denoted by ‘with WIC’) for the tunnel wall effects to represent the free-air results and uncorrected (denoted by ‘without WIC’) for the tunnel wall effects. The effects of tunnel walls on the measured surface pressure coefficients appear to be insignificant at all stations over the main wing. In general, the CFD results show very small

variations in the computed surface pressures among all the cases studied; they correlate well with the measured data over the main wing. In particular, the CFD prediction of the suction peak associated with the flow expansion at LEF hinge-line is very good. The computed pressures also show evidence of flow expansion at the shroud hinge-line and around the leading edge of the TEF. The small disagreements between the CFD results and the data over the aft part of the main inboard-wing lower surface (3 to 4 pressure tap locations are misaligned from the constant span-wise stations) are due to the TEF bracket hardware on the wind-tunnel model. These two brackets (see figure 2) are not numerically modeled. The CFD results for the MIT and MIF show small variations in the computed pressures around the leading edge of the deflected flap over the wing outboard panel.

The computed upper surface pressures over the TEF at station $Y/(b/2)=0.45$ indicate a significant loading due to a vortex flow that emanates from flap side-edge. The effect of this vortex flow and the resulting low pressure-field on the upper surface of the TEF was shown earlier in figure 14. It should be noted that this effect, discussed in the next paragraph, is also seen in the measured surface pressure data, although not compared directly with CFD results due to the X/c mapping inconsistencies discussed earlier.

The distribution of the experimental surface pressure coefficients measured over the shroud and TEF, that have been corrected for the tunnel wall interference effects, are shown in figure 19. These pressure distributions are plotted in a different reference coordinate system and scale (i.e., stretched horizontal axis) than the corresponding CFD results shown for the shroud and TEF in the previous figure. The measured data clearly show similar trends, to the CFD results, in chordwise pressure loading over the shroud and in particular over the TEF. At the inboard stations, the TEF pressure distributions show an attached flow. At the outboard station, the pressure distribution shows two suction peaks; one is located just aft the leading edge due to the leading-edge flow expansion and subsequent

acceleration through the gap/overlap opening, and the other is located further aft due to the presence of side-edge vortex flow.

Force and Moment: The computed overall lift, drag, and pitching moment coefficients are shown in figure 20 along with the corresponding NTF experimental data with and without WIC application. The close-up views of each respective data set near the flow conditions of interest are shown in the right-hand column. Consistent with the experimental data, it is important to note that the contributions from the standoff geometry and the blunt fuselage-base are excluded from all the computed coefficients. The experimental lift coefficients indicate a fairly linear variation with angle of attack, and as expected the application of WIC to account for the tunnel wall interference results in a decrease in lift curve slope.

The computed lift coefficients from the MIT and MIF agree well with the measured data, especially the increments due to WIC (see the close-up results). The overall magnitudes are slightly over-predicted by about 0.01. Also the MIF computed lift coefficient at $\alpha_c=10.6^\circ$ correlates well with the corrected NTF data. As a result, the lift curve slope for the free-air computations (i.e., MIF and MIF at $\alpha_c=10.6^\circ$) is also predicted well. Extracting the standoff geometry physically from the numerical model causes only a small decrease in the MNIF computed lift coefficient relative to the MIF prediction and it compares very well with the corrected NTF data.

The measured pitching moment characteristics exhibit very little change at low to moderate C_L range, followed by a nose down tendency with increasing C_L . The experimental data also indicate diminutive effects from the application of WIC method on the overall pitching moment characteristics. The correlation of the computed pitching moments with experimental data is reasonable, though the enlarged plot on the right-hand column may be misleading because of the expanded scales. Nonetheless, the predicted trend (i.e., $\Delta C_m/\Delta C_L$) for the free air computations is not

predicted well.

The measured drag polar indicates the expected trend and that the modification due to WIC application appears to become more pronounced with increasing C_L . The computed drag coefficients are in general agreement with the experimental measurements in terms of the trends but not the magnitude. Also note the increase in the predicted drag coefficient (~55 counts) with MNIF computation compared to the MIF result. In addition to the obvious geometrical differences between the two models (i.e., standoff), there is also the different imposed boundary conditions on the configuration plane-of-symmetry. In an effort to determine a possible source for this drag change, further diagnostic analysis was performed as discussed in the following section.

Sidewall/Standoff Interference Analysis

The predicted drag coefficients from MIF and MNIF computations are shown in figure 21 along with the results for the other two CFD cases for completeness. The drag coefficients are plotted against the block number in the computational domain. With the exception of the first two blocks that define the configuration forebody longitudinally up to the fuselage/wing-LE juncture point, the results indicate that the computed drag remains fairly unchanged for the remaining blocks. The majority of the increase in MNIF computed total drag, relative to MIF results, is attributed to the configuration forebody (about 40 counts) and the wing components (about 10 counts). This effect is likely to be associated with the standoff geometry and the boundary condition imposed on the wall to which the model is mounted, i.e., viscous wall for MIF and inviscid symmetry plane for MNIF. As a result, the configuration forebody experiences a different flow field in MIF computations compared to the MNIF as will be explored in the following paragraphs. This difference in the computed drag coefficients may become important, particularly when it is applied to semispan experimental data reduction towards

obtaining full configuration data. Similar data analysis was also performed for the computed lift coefficients that indicated negligible variations in all blocks with the exception of the wing components where they showed slight variations.

Computed pressure distributions along the fuselage centerline (i.e., fuselage and standoff boundary line, $Y=0$ mm) are shown in figure 22. The results clearly indicate very small differences between all the computations with the exception of the MNIF solutions over the configuration forebody. The majority of the differences occur roughly over the front one-third of the fuselage where the MNIF predicted pressures appear to exhibit less suction on the upper surface and more compression on the lower surface. As expected, only the computed pressure coefficients with MNIF indicate a stagnation point (i.e., $C_p \sim 1.0$) on the forebody unlike all the other solutions where their respective pressure coefficients do not exceed 0.83. The bulging of the pressure distribution in the mid-fuselage region ($0 < X < 1200$) is attributed to the wing pressure field propagation inboard onto the fuselage. It is also interesting to note that the fuselage pressure distributions indicate a rapid decrease and increase in pressures, near the fuselage base on the upper and lower surfaces, respectively. This abrupt change in the fuselage pressure difference near the base plane is likely caused by the flow separation at the sharp corners of the base resulting in a wake-like flow-field behind the blunt face of the fuselage. The cross sectional pressure distribution on the forebody is analyzed next to identify the circumferential extent of the pressure difference between MNIF and the other CFD results.

The computed circumferential pressure distribution at two fuselage cross sections of $X=-500$ mm and $X=-200$ mm are shown in figure 23. The first cross section is very close to the fuselage nose (see figure 22 for relative location with respect to the overall fuselage length) and the second station is roughly about the mid-forebody. The figure also shows the corresponding cross-sectional geometry including the standoff component hash-marked for

reference. The results clearly indicate that the pressure difference observed between the MNIF and the other CFD solutions on the forebody is not confined to the fuselage centerline but it also manifests itself circumferentially at both stations. There are two primary factors that contribute to this forebody pressure difference and the resulting computed drag coefficients (figure 21). The first factor is the standoff geometry itself that results in an increase in the cross-sectional area of the forebody, particularly near the nose. From a slender body theory perspective, this area effect would shift the pressures negatively without changing the sectional load. The pressure difference on the forebody (figure 23) shows this shows this type of slender-body-theory trend, although the precise magnitudes of the offset would be affected by the presence of the viscous sidewall boundary layer. The second factor is associated with the detailed flow within the sidewall boundary layer as discussed in the next paragraph.

The computed total velocity vectors (at the second grid points normal to the surface) along with surface pressure coefficients on the tunnel sidewall (only a portion of which is shown) and standoff obtained from the MIF solutions are shown in figure 24(a). The figure also shows the off-surface particle traces released at key locations to capture the presence of the horseshoe vortex that develops in front of the blunt face of the standoff geometry. The entire vortex appears to be imbedded within the sidewall boundary layer and stays within it after splitting around the forebody as shown in a close-up view from an oblique angle in figure 24(b). The core of this horseshoe vortex, at the point where it splits around the forebody, is ~ 20 mm upstream of the standoff nose and ~ 5 mm off the tunnel sidewall. Further analysis indicates that at a short distance downstream of the forebody apex, both branches of this horseshoe vortex (above and below the standoff) becomes squeezed and gets closer to the sidewall and finally diffuse into the stream-wise flow. The low-pressure suction peaks (above and below the standoff) associated with this horseshoe vortex are also evident at station $X=-500$ mm in figure 23. However, such suction peaks are

clearly not present over the standoff at forebody station $X=-200$ mm.

Complementary to the surface pressure comparison at the fuselage centerline (i.e., figure 22), figure 25 shows the difference in the computed pressure coefficients across the symmetry plane between the MIF and MNIF solutions. The grids are shown for only a portion of tunnel sidewall and for every three points in both directions for clarity. This result clearly shows the field effect due to the presence of the sidewall boundary layer (causing the formation of the horseshoe vortex) and standoff geometry across the fuselage centerline plane. Similar to the earlier findings, this result also indicates that the majority of the pressure difference between the two solutions is confined only on and around the forebody region where the flow compression ahead of the forebody is followed by the flow expansion around it. At this angle of attack, this pressure-field expansion around the forebody, on the top and bottom portion, appears to be symmetric (i.e., counteracting effect) which results in only a small contribution to the overall lift characteristics. However with increasing angle of attack, the BL horseshoe vortex and the resulting pressure-field expansion across the configuration symmetry plane may not remain symmetric thus causing a higher normal force to be produced by the forebody. It should be noted that this additional normal force is measured by the model balance as part of the configuration overall aerodynamic performance.

Conclusions

The results from a numerical study for the NTF semispan diamond wing model are presented for low-speed, high-lift conditions. The CFD results are based on the solutions to the Reynolds-averaged Navier-Stokes equations that are solved in a multiblock structured-grid computational domain. The computations utilize the Spalart-Allmaras model to account for the turbulent effects in the flow. The CFD study consisted of four cases: NTF empty tunnel flow simulation, model/standoff in the tunnel (MIT), model/standoff in free-air (MIF), and model/no-

standoff in the free-air (MNIF). The computations focused on a configuration with the high-lift rigging arrangement designed for landing approach at nominal flow conditions of $\alpha=10^\circ$, $M_\infty=0.2$, and $R_\infty=24.2 \times 10^6$. A typical volume grid (MIT) consisted of about 7 million grid points and the computations required about 300 MW of memory and 60 hours of CPU time of a single processor on a Cray C-90 platform.

An approach based on flat plate theory was developed to determine an upstream extension to the nominal NTF test section for better simulation of the tunnel sidewall boundary layer flow characteristics. The validity of the approach was later assessed by applying the turbulent Navier-Stokes method to simulate the empty tunnel flow field. The resulting sidewall boundary-layer flow was shown to correlate very well with the available experimental rake measurements. Empty tunnel flow simulation results revealed that an upstream extension (~ 15 ft) to the nominal NTF test section (25 ft), as an approximate replacement for the tunnel settling chamber and the contraction cone geometry, was adequate for modeling of the tunnel sidewall boundary-layer flow characteristics.

The ability of the method to simulate the complex flow structures on the diamond wing high-lift model at low-speed flow conditions for MIT, MIF, and MNIF was demonstrated. The general flow features of the configuration include: attached flow over the majority of the lifting surfaces, the flow separation from the TEF side-edge forming a vortex system, low momentum vortex-like flow trapped in the cove region, and a trailing- wake flow-field behind the blunt fuselage base. In general from a high-lift design standpoint, the computed flow characteristics indicated that the desired attached flow was successfully maintained over the majority of the aerodynamic surfaces at these conditions. Experimental data for the detailed flow physics are not available to assess the accuracy of the predicted flow structures in different regions of the domain. However, the predicted results are correlated with the measured surface pressure distribution and the overall forces and moment.

Negligible difference was shown to exist between the experimentally corrected and uncorrected wing pressures to account for the wall interference effect. The numerical results also showed small changes on the wing surface pressure distributions due to the tunnel wall confinement effects as well as the combined tunnel sidewall boundary layer and standoff effects. In general, the computed surface pressure distribution over the wing compared reasonably well with the available experimental data.

The numerical predictions for the overall forces and pitching moment are shown to correlate reasonably well with the NTF measured data with and without the correction for the tunnel wall interference effects. In particular, a very good agreement between the computed lift coefficients and the measured data are obtained both in terms of magnitudes and the increments due to wall interference effects. Elimination of the standoff geometry from the numerical model is shown to slightly decrease the configuration overall lift coefficient computed for free-air simulation. The computed drag coefficients are in general agreement with the experimental measurements in terms of the overall trends, incremental shift due to wall interference effects, but not the magnitudes. The agreement in overall trends include the slope in drag-polar curve (i.e., MIF and MIF at $\alpha_c=10.6^\circ$ data points). Compared to the MIF prediction, the MNIF computed drag coefficient indicated an increase of about 55 counts that is shown to primarily arise from the configuration forebody (about 40 counts) and main wing components (about 10 counts). The change in computed drag-coefficient is attributed to the obvious differences between the two models; they are the standoff geometry and the sidewall BL effects. Furthermore, the computed forebody pressures from MNIF case clearly indicated differences with those computed from MIT, MIF, and MIF (at $\alpha_c=10.6^\circ$).

Detailed flow field analysis revealed insight into the flow characteristics of the combined sidewall boundary layer and the standoff effects around the forebody that led to possible explanations for the drag increase in the MNIF

computation. It is demonstrated that such combined effects cause a pressure characteristic in the fuselage centerline plane (i.e., plane-of-symmetry) that is different than the one computed for the full span configuration (i.e., MNIF). This undesirable pressure difference in the plane-of-symmetry between the MIF and MNIF solutions is confined mainly to the configuration forebody region. This pressure difference is attributed to the presence of a horseshoe vortex as well as the standoff geometry that effectively increases the fuselage span and thus changing the local flow characteristics. These results clearly suggest that in order to improve the flow characteristics in the fuselage centerline plane of a semispan model, one may need to focus on improving a standoff design shape around the forebody region. Furthermore, such design endeavor should include not only surface flow properties but perhaps flow field properties as well to capture the flow non-linearity due to the presence of the horseshoe vortex and the resulting aerodynamic effects.

References

1. Takallu, M.A., Laflin, K.R.: Reynolds-Average Navier-Stokes Simulations of Two Partial-Span Flap Wing Experiments. AIAA Paper No. 98-0701, January 1998.
2. Berkman, M.E., Khorrami, M.R., Choudhari, M., Sadowski, S.S.: Investigation of High-Lift Flow Field of an Energy Efficient Transport Wing. AIAA Paper No. 99-0926, January 1999.
3. Rogers, S.E., Roth, K., Cao, H.V., Slotnick, J.P., Whitlock, M., Nash, S.M., Baker, M.D.: Computation of Viscous Flow for a Boeing 777 Aircraft in Landing Configuration. AIAA Paper No. 2000-4221, August 2000.
4. Mavriplis, D.J., Pirzadeh, S.: Large-Scale Parallel Unstructured Mesh Computations for 3D High-Lift Analysis. AIAA Paper No. 99-0537, January 1999.
5. Ghaffari, F.: Unstructured Grid Viscous Flow Simulation Over High-Speed Research Technology Concept Airplane at High-Lift

- Conditions. NASA/TP-1999-209718, November 1999.
6. Wahls, R. A.: The National Transonic Facility: A Research Retrospective. AIAA Paper No. 2001-0754, January 2001.
 7. Luckring, J.M., Ghee T.A.: Subsonic Reynolds Number Effects on a Diamond Wing Configuration. AIAA Paper No. 2001-0907, January 2001.
 8. Iyer, V., Everhart, J.L., Bir, P.J., Ulbrich, N.: Implementation of WICS Wall-Interference Correction System at the National Transonic Facility. AIAA Paper No. 2000-2383, June 2000.
 9. Gatlin, G.M., Parker, P.A., and Owens, Jr., L.R.: Development of a Semispan Test Capability at the National Transonic Facility. AIAA Paper No. 2001-0759, January 2001.
 10. Milholen II, W. E.: A Design Methodology for Semispan Model Mounting Geometries. AIAA Paper No. 98-0758, January 1998.
 11. Krist, S. L., Biedron, R. T., and Rumsey, C. L.: CFL3D User's Manual (Version 5.0), NASA TM-1998-208444, June 1998.
 12. Spalart, P.R., Allmaras, S.R.: A One-Equation Turbulence Model for Aerodynamic Flows. *La Recherche Aerospatiale*, No. 1, 1994, pp. 5-21.
 13. Ghee, T.A. and Taylor, N.J.: Low-speed Wind Tunnel Tests on a Diamond Wing High-Lift Configuration. AIAA Paper No. 2000-4507, August 2000.
 14. Burner, A., Liu, T., Garg, S., Ghee, T.A., Taylor, N.J.: Aeroelastic Deformation Measurements of Flap, Gap, and Overhang on a Semispan Model. AIAA Paper No. 2000-2386, June 2000.
 15. Bobbitt, C., Jr., Everhart, J.L., Foster J., Hill, J., McHatton, R., and Tomek, W.: National Transonic Facility Characterization Status. AIAA Paper No. 2000-0293, January 2000.
 16. Thomas, J.L., Newsome, R.W.: Navier-Stokes Computations of Lee-Side Flows Over Delta Wings. AIAA Paper No. 86-1049, May 1986.
 17. Thomas, J.L., Taylor, S.L., Anderson, W.K.: Navier-Stokes Computations of Vortical Flows Over Low Aspect Ratio Wings. AIAA Paper No. 87-0207, January 1987.
 18. Vatsa, V.N., Thomas, J.L., and Wedan, B.W.: Navier-Stokes Computations of Prolate Spheroids at Angle of Attack. AIAA Paper No. 87-2627, August 1987.
 19. Biedron, R.T., Thomas, J.L.: A Generalized Patched-Grid Algorithm With Application to the F-18 Forebody With Actuated Control Strake. *Comput. Sys. Eng.*, Vol. 1, nos. 2-4, 1990, pp. 563-576.
 20. Thomas, J.L., Walters, R.W., Taekyu, R., Ghaffari, F., Weston, R.P., Luckring, J.M.: A Patched-Grid Algorithm for Complex Configurations Directed Towards the F/A-18 Aircraft. AIAA Paper No. 89-0121, January 1989.
 21. McMillin, S. N., Thomas, J. L., Murman, E.M.: Navier-Stokes and Euler Solutions for Lee-Side Flows Over Supersonic Delta Wings – A Correlation With Experiment. NASA TP-3035, 1990.
 22. Ghaffari, F., Luckring, J. M., Thomas, J. L.: An Overview of the Navier-Stokes Computations About the F/A-18 Aircraft With Multiblock Structured Grids. *Proceedings from High-Angle of-Attack Technology, Accomplishments, Lessons Learned, and Future Directions*. NASA Langley Research Center, Sept. 17-19, 1996. NASA/CP-1998-207676/PT3. pp. 1261-1296, June 1998.
 23. Roe, P. L.: Characteristic-Based Schemes for the Euler Equations. *Annual Review of Fluid Mechanics*, Volume 18, Milton van Dyke, J. V. Wehausen, and John L. Lumley, Eds. Annual Reviews Inc., 1986, pp. 337-365.
 24. Rumsey, C. L., Allison, D. O., Biedron, R. T., Buning, P. G., Gainer, T. G., Morrison, J. H., Rivers, S. M., Mysko, S. J., Witkowski, D. P.: CFD Sensitivity Analysis of a Modern Civil Transport Near Buffet-Onset Conditions. NASA/TM-2001-211263, December 2001.

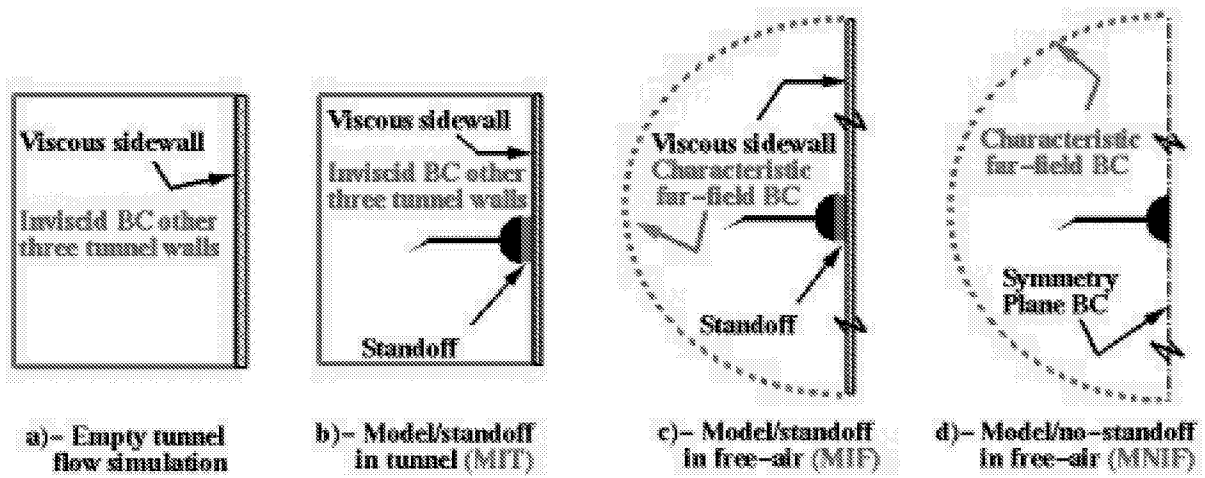


Figure 1. CFD plan for the NTF diamond wing semispan model.

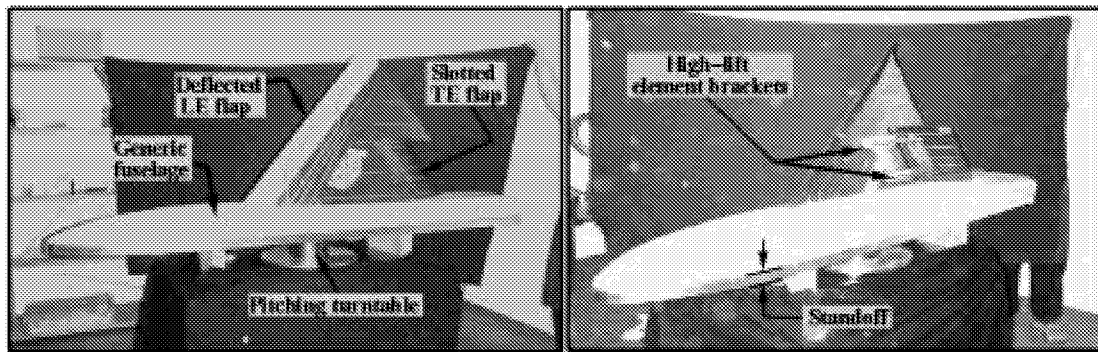
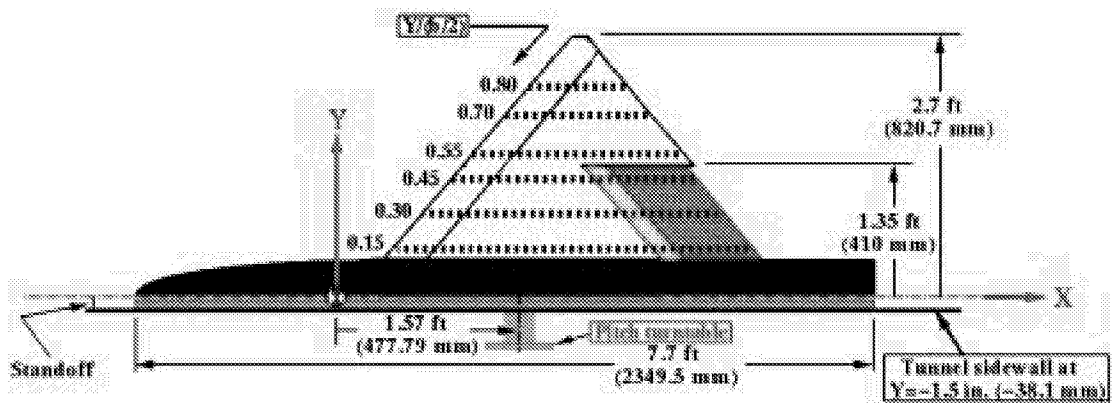
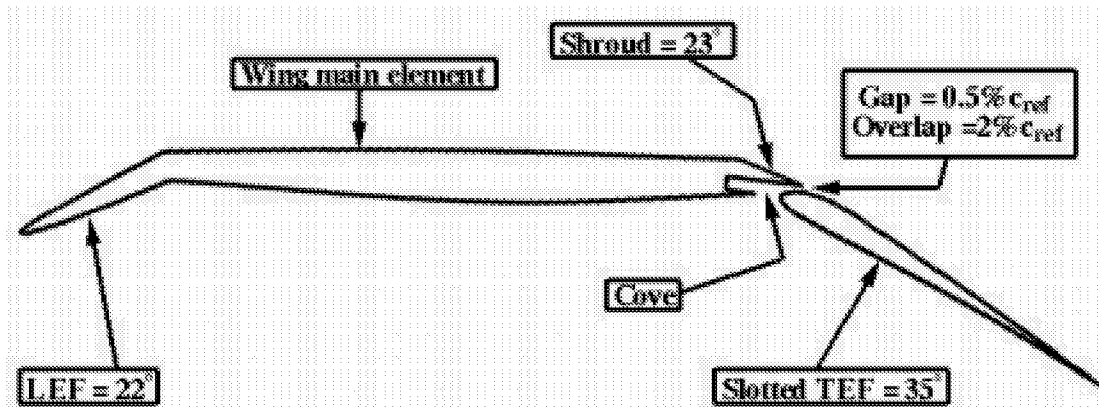


Figure 2. Diamond wing semispan model.



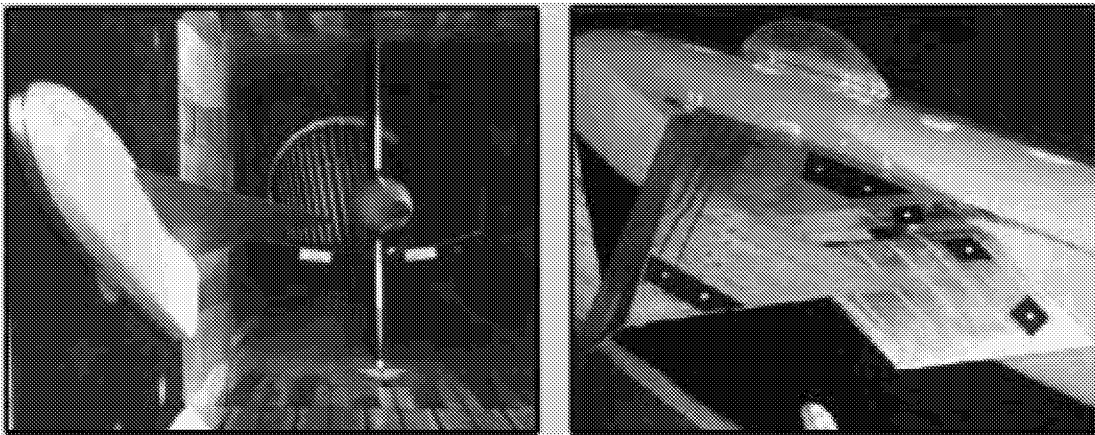
(a) Model planform and pressure measurement stations.

Figure 3. Wind-tunnel model geometry attributes.



(b) Baseline high-lift wing sectional-cut.

Figure 3. Concluded.



(a) Cruise wing configuration.

(b) High-lift configuration.

Figure 4. Diamond wing semispan model mounted on the NTF tunnel sidewall.

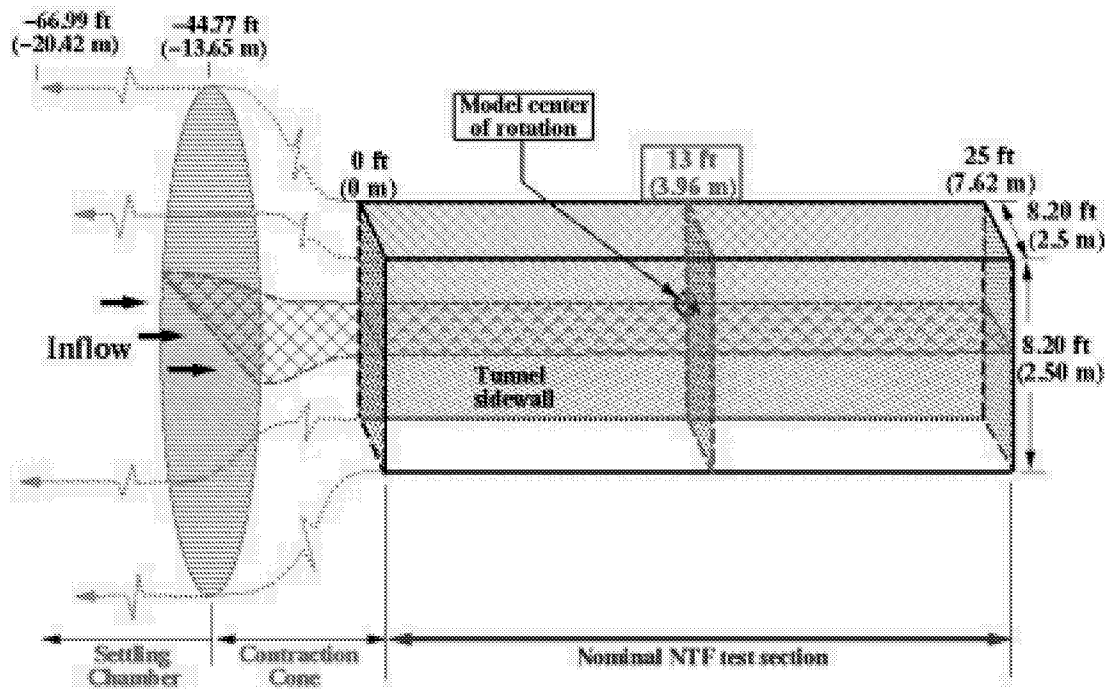
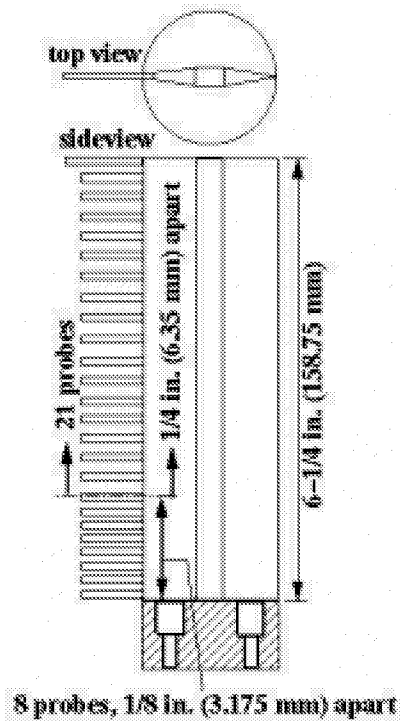
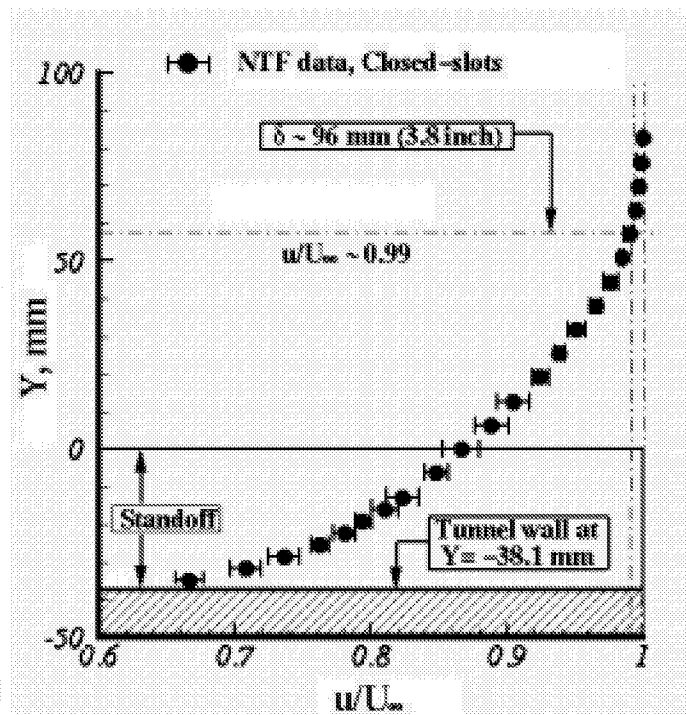


Figure 5. Schematic view of the NTF wind tunnel.



(a) Rake apparatus.



(b) Measured BL velocity profile.

Figure 6. Schematic view of the BL rake and the sidewall measured BL velocity profile at the model center of rotation.

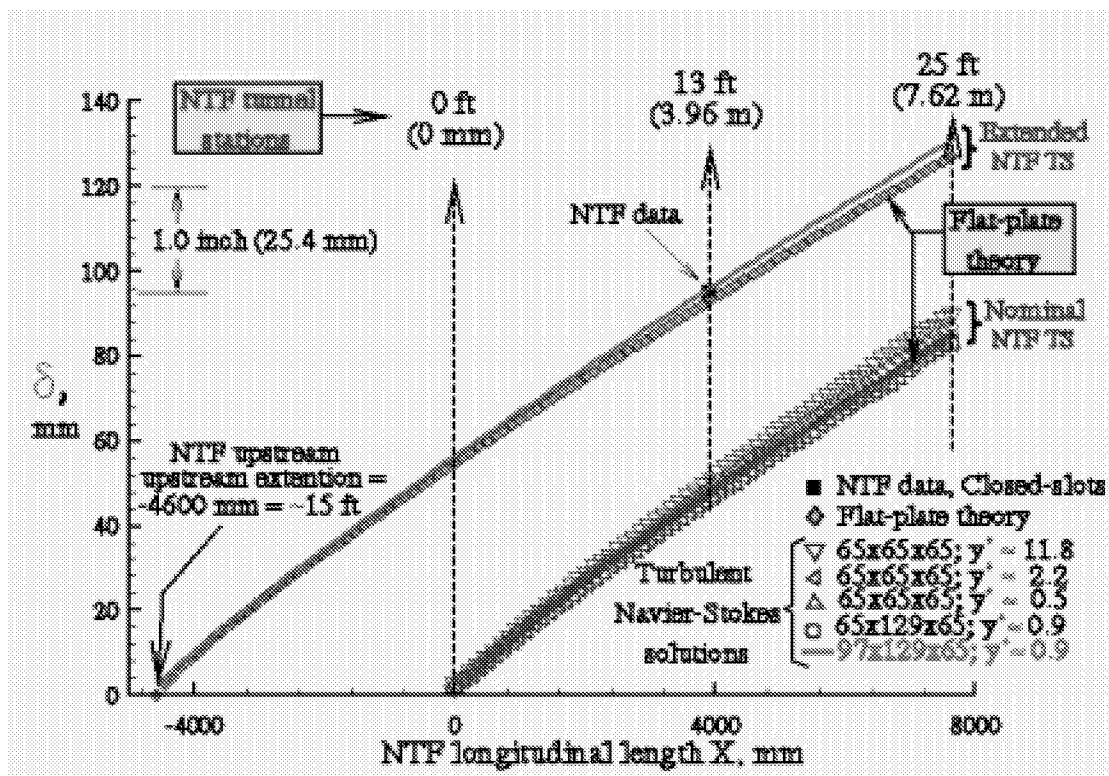


Figure 7. Computed Navier-Stokes, flat-plate theory and measured boundary-layer growth along NTF sidewall.

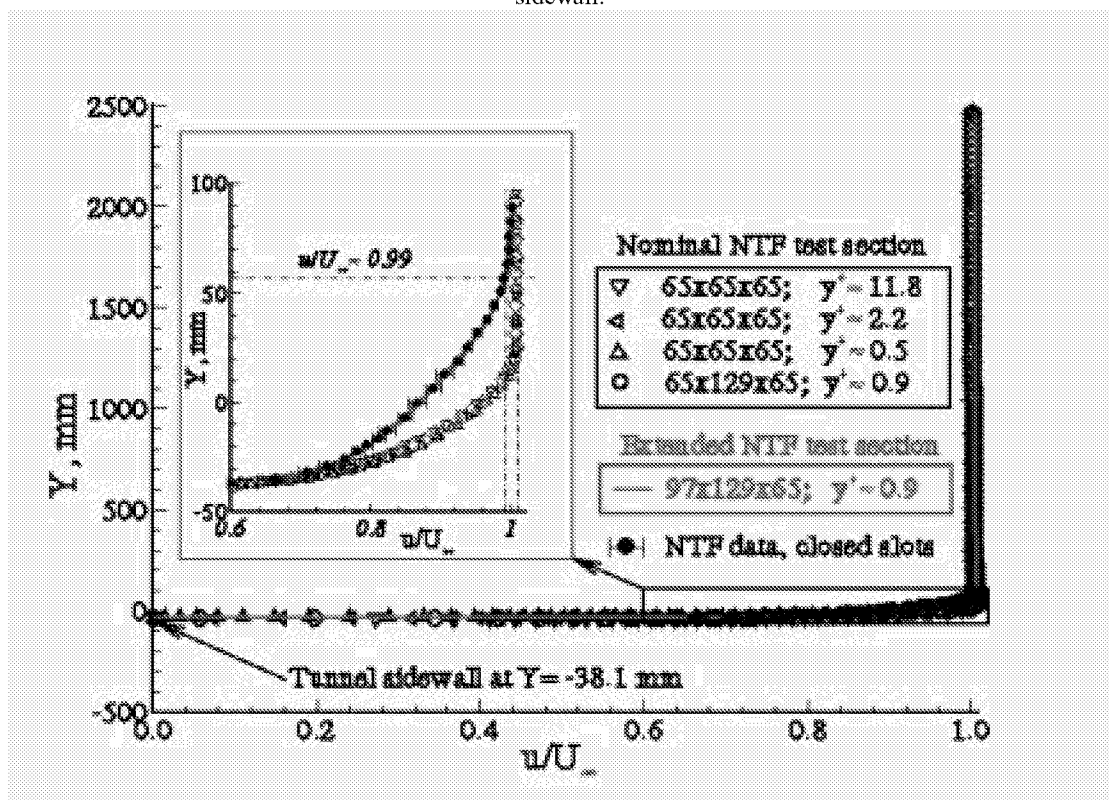
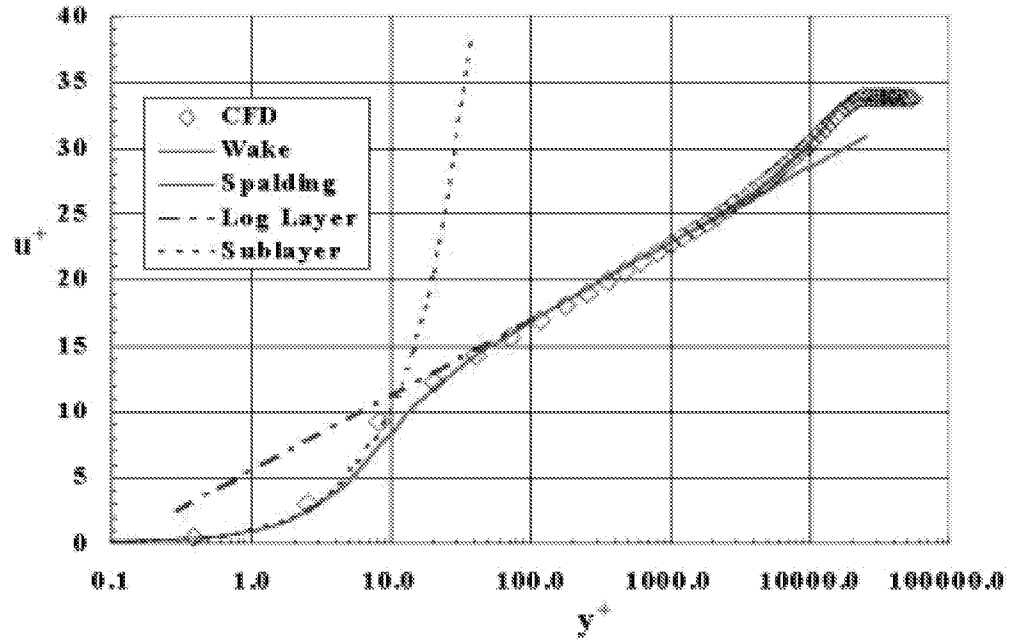
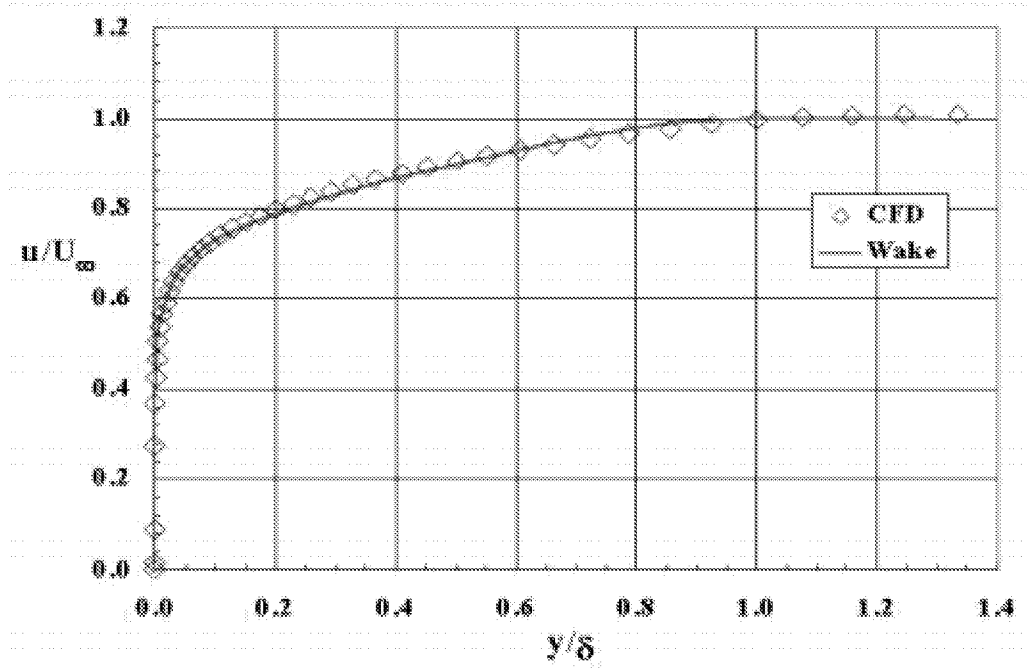


Figure 8. NTF sidewall computed and measured axial velocity profile at the model center of rotation.



(a) Sidewall boundary layer profile in inner law variables at the model center of rotation.



(b) Sidewall boundary layer profile at the model center of rotation.

Figure 9. Comparison of the computed CFD results with the law of the wall theory.

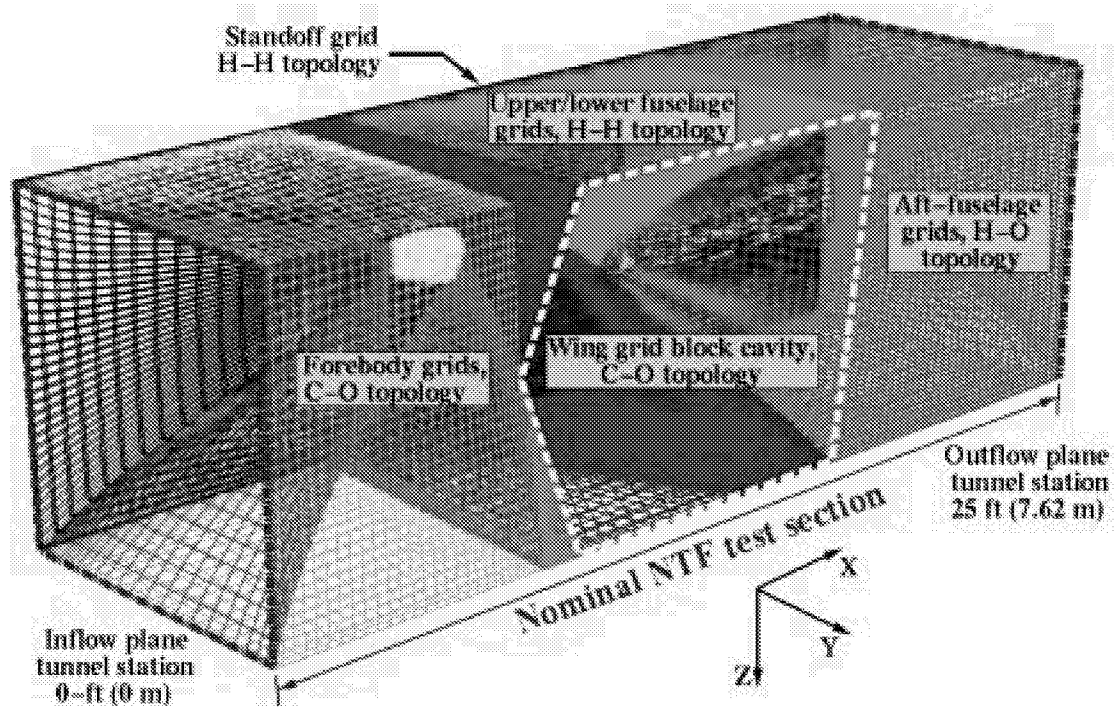


Figure 10. Grid topology for the Model/Stand-off in the nominal NTF test section.

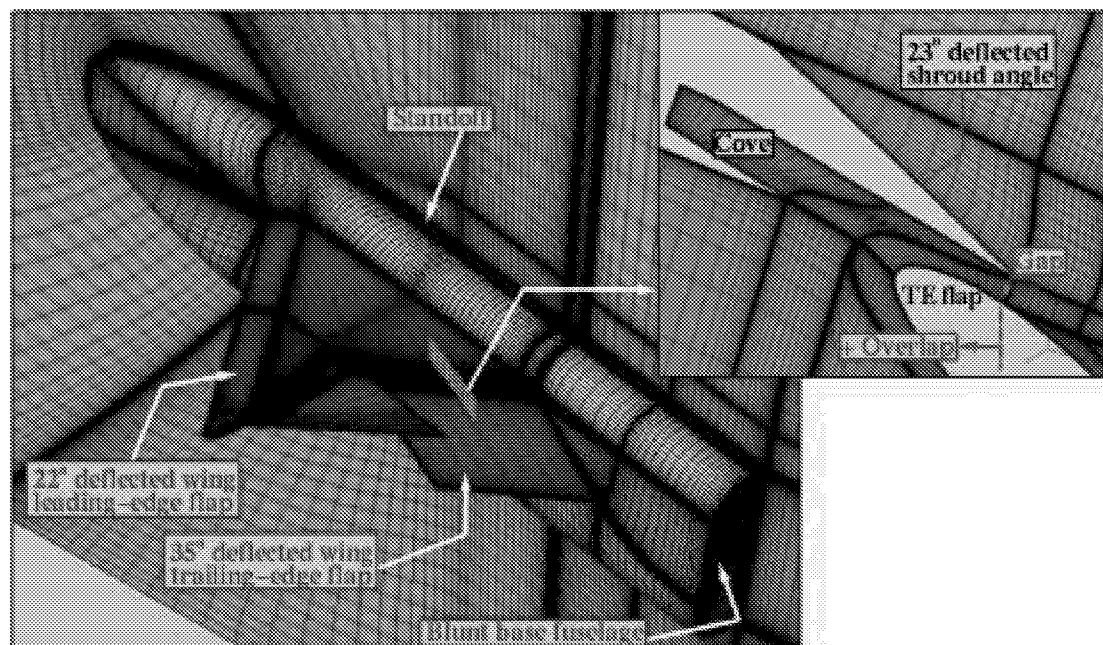
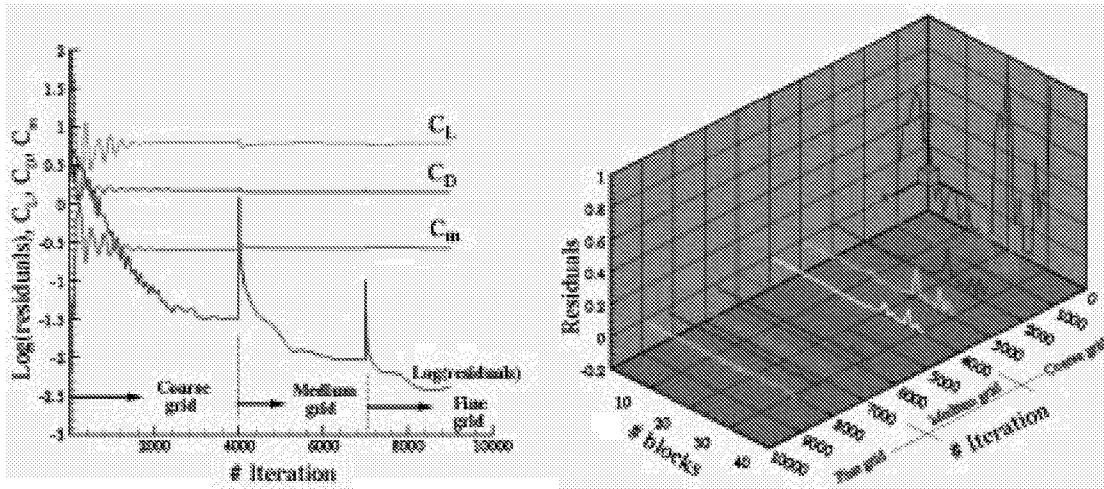


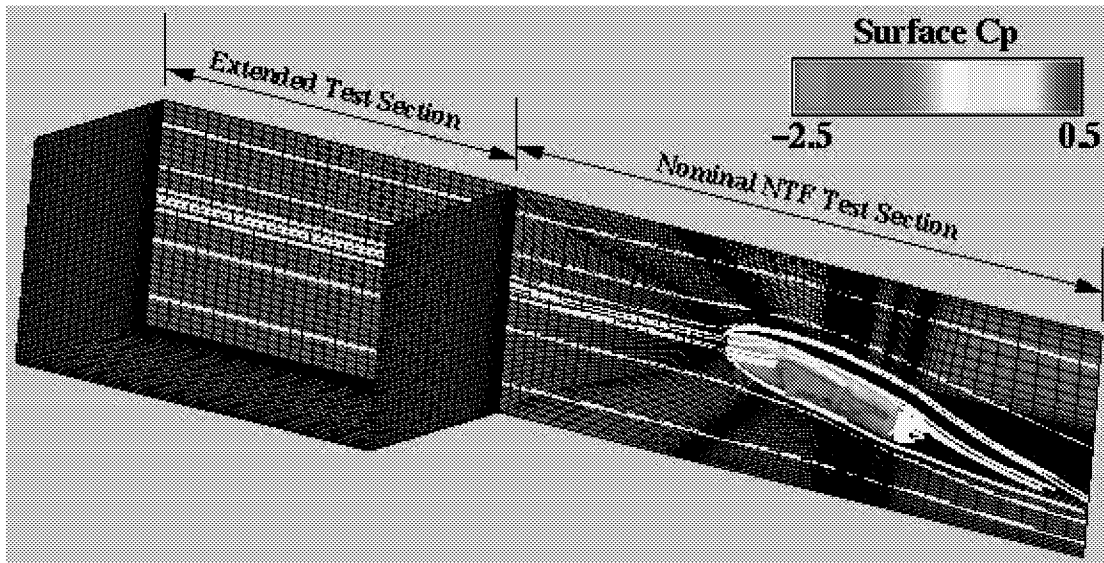
Figure 11. Close-up view of the semispan diamond wing numerical model mounted on the NTF tunnel sidewall.



(a) Overall solution convergence characteristics.

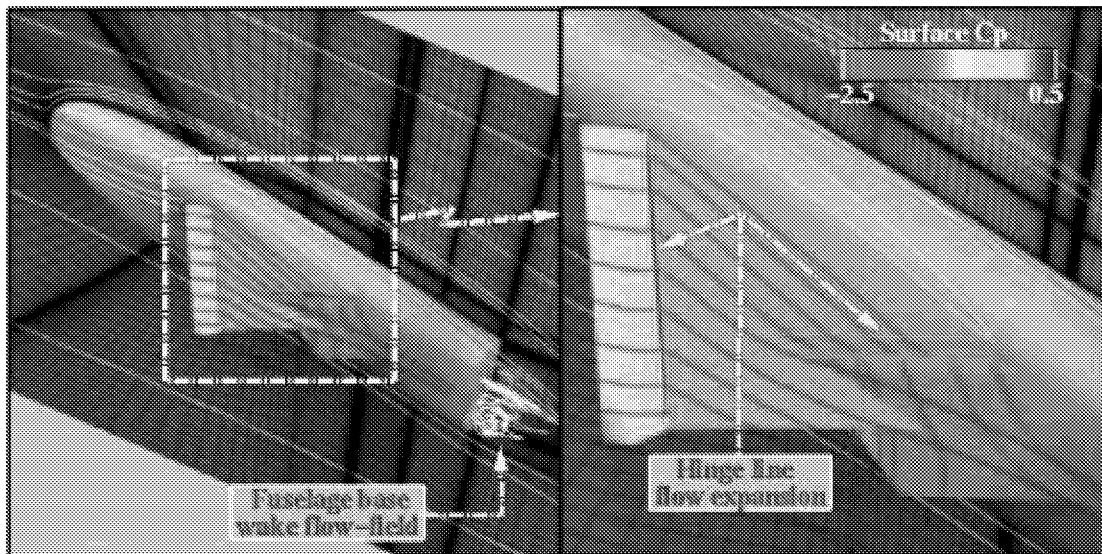
(b) Grid block residual variations.

Figure 12. Solution convergence characteristics for the MIT case.

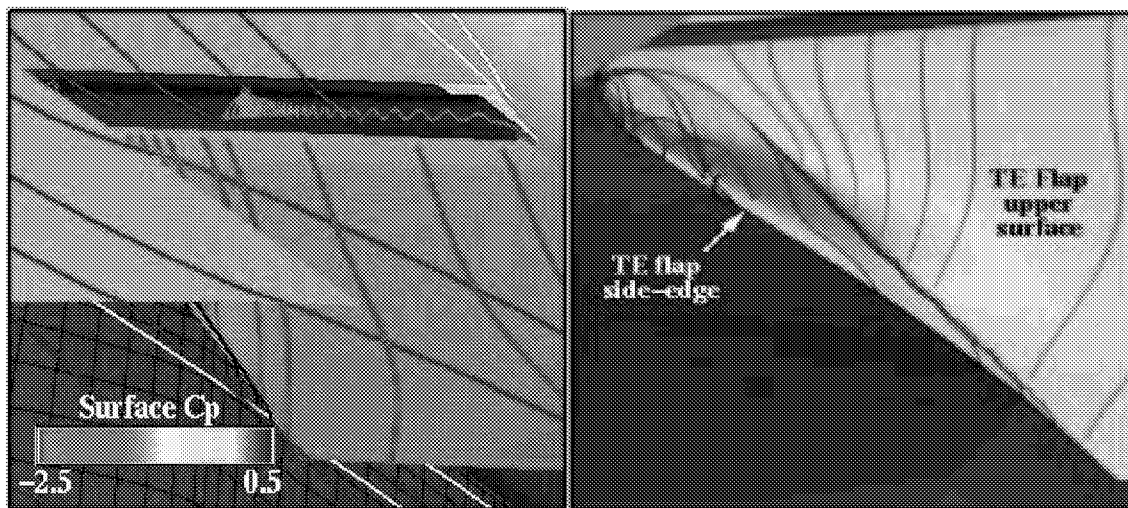


(a) Overall view of the solution.

Figure 13. Turbulent Navier-Stokes flow field simulation for the model in the extended NTF test section.

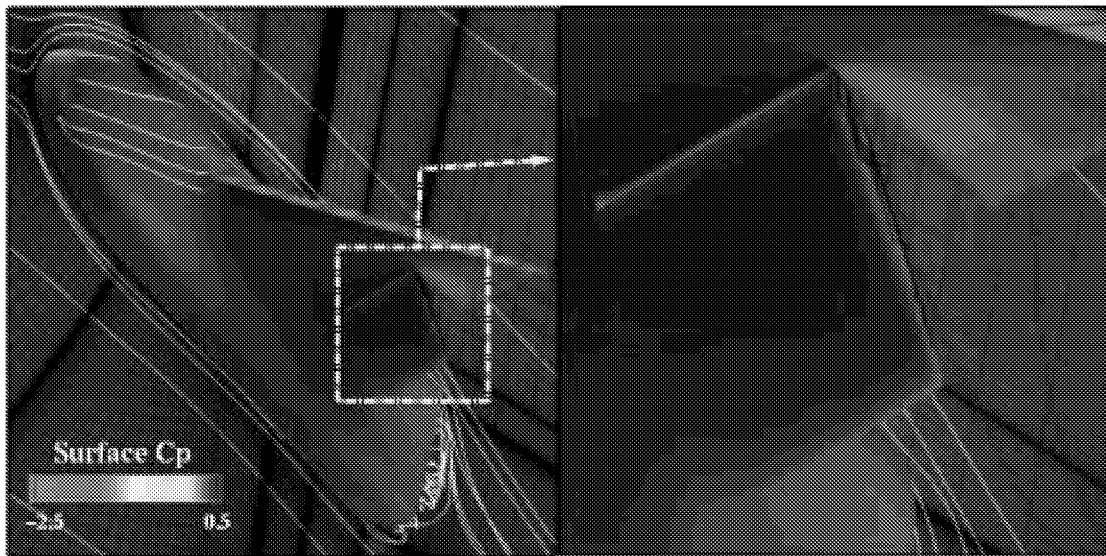


(b) Close up of the upper surface C_p and streamlines over the model and the wing.



(c) Close up of the upper surface C_p and streamlines in the cove region and around the TEF side-edge.

Figure 13. Continued.



(d) Close up view of the lower surface C_p and streamlines over the model and TEF component.

Figure 13. Concluded.

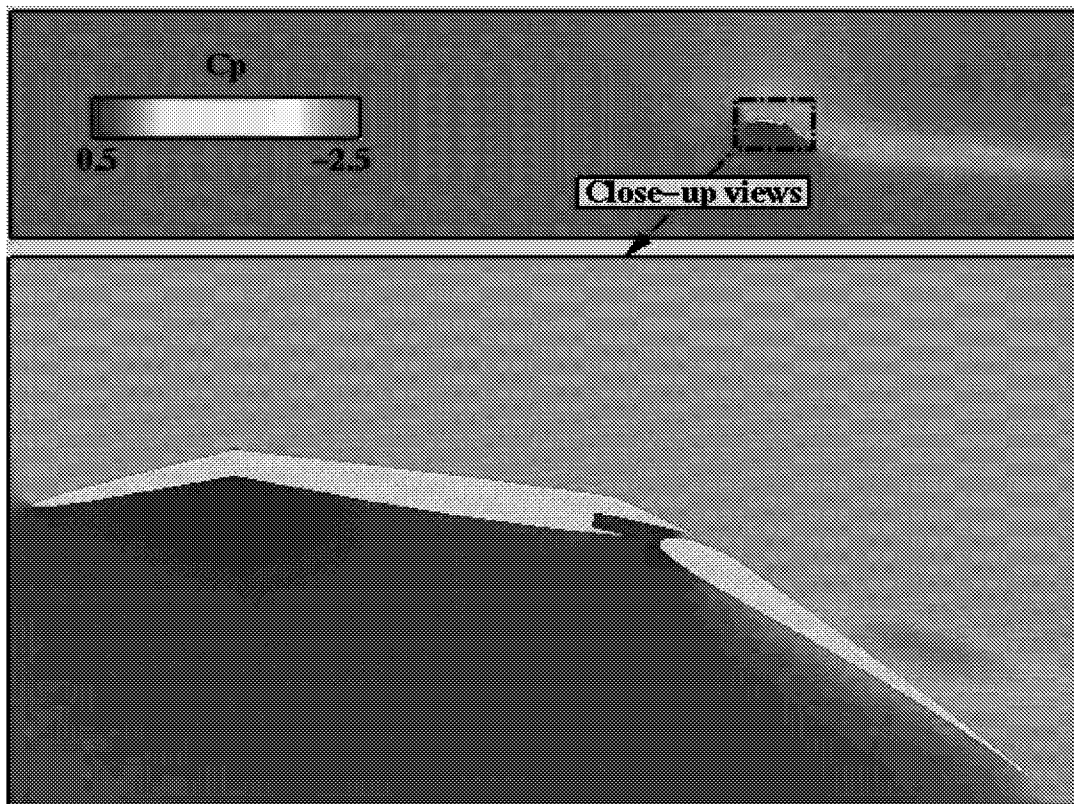


Figure 14. Longitudinal cut through the MIT computed pressure field at $Y=1.33$ ft (405 mm).

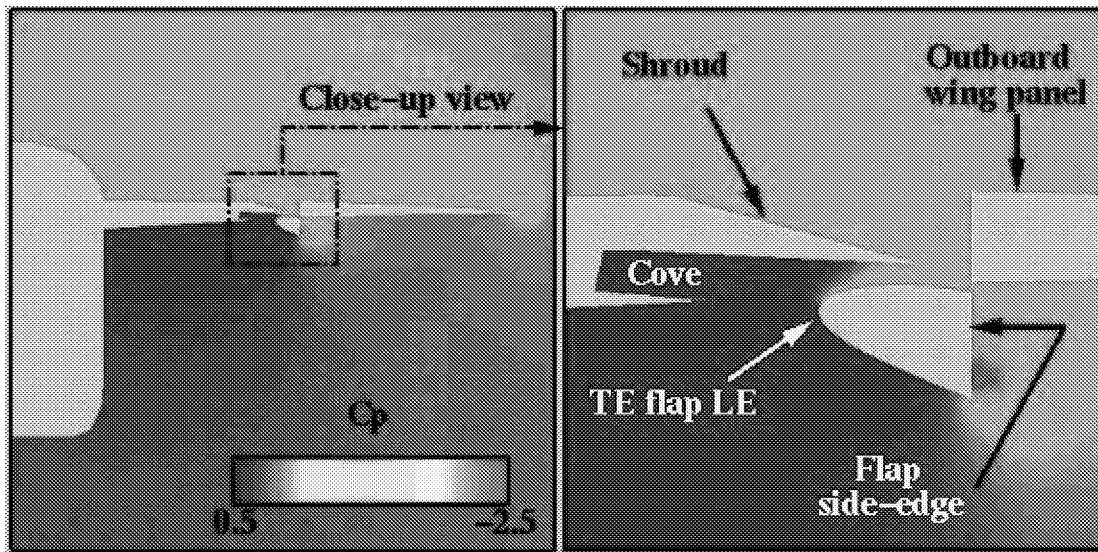


Figure 15. Lateral cut through the MIT computed pressure field at X=2.74 ft (835 mm).

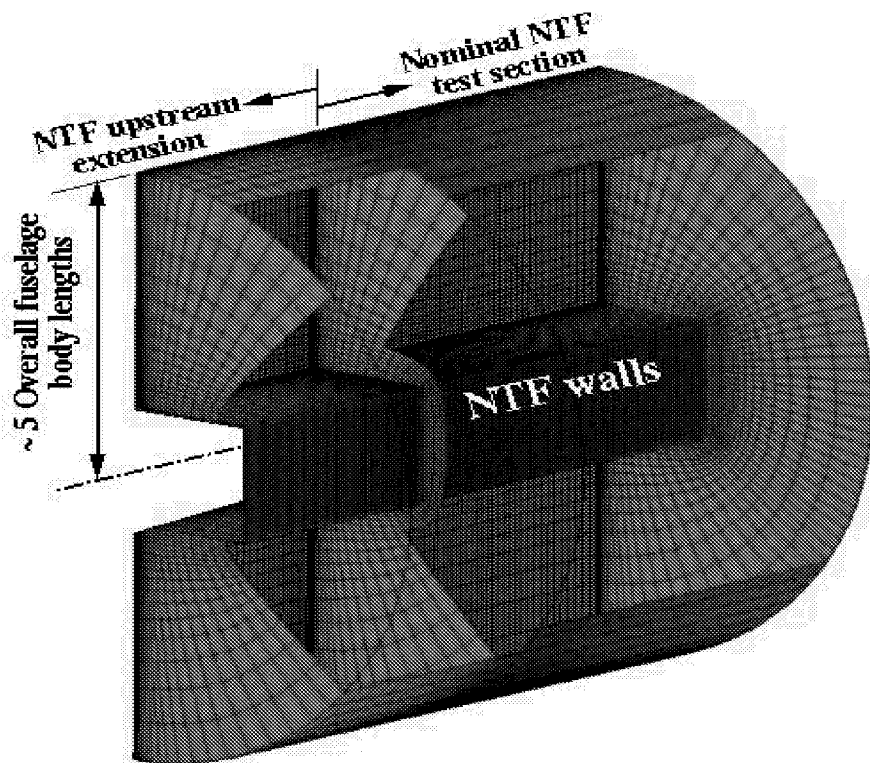
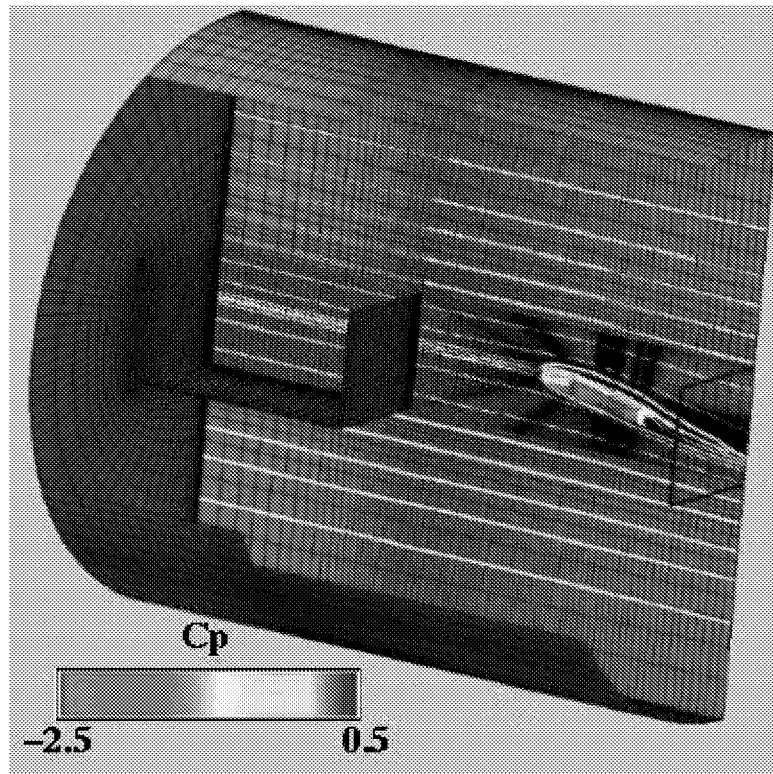
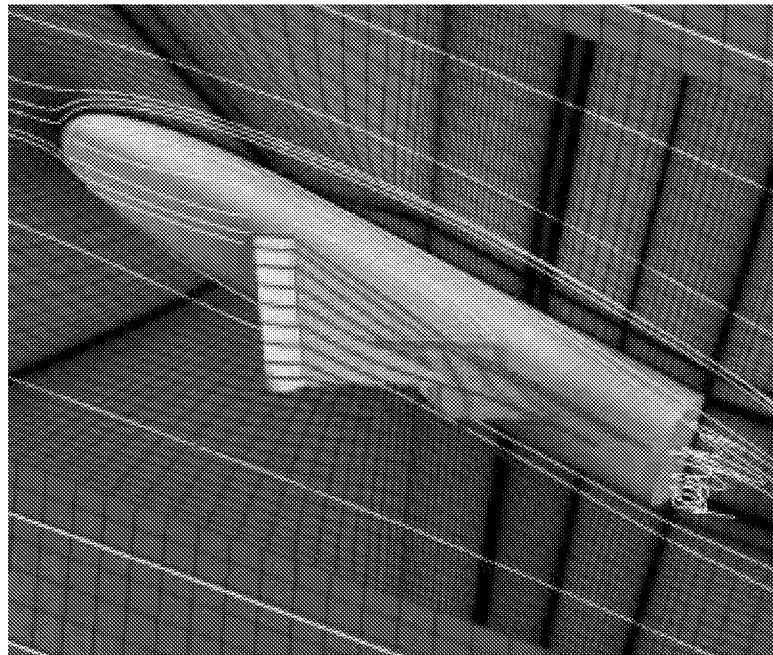


Figure 16. Exterior grid wrapping around the MIT grid for developing the MIF grid.

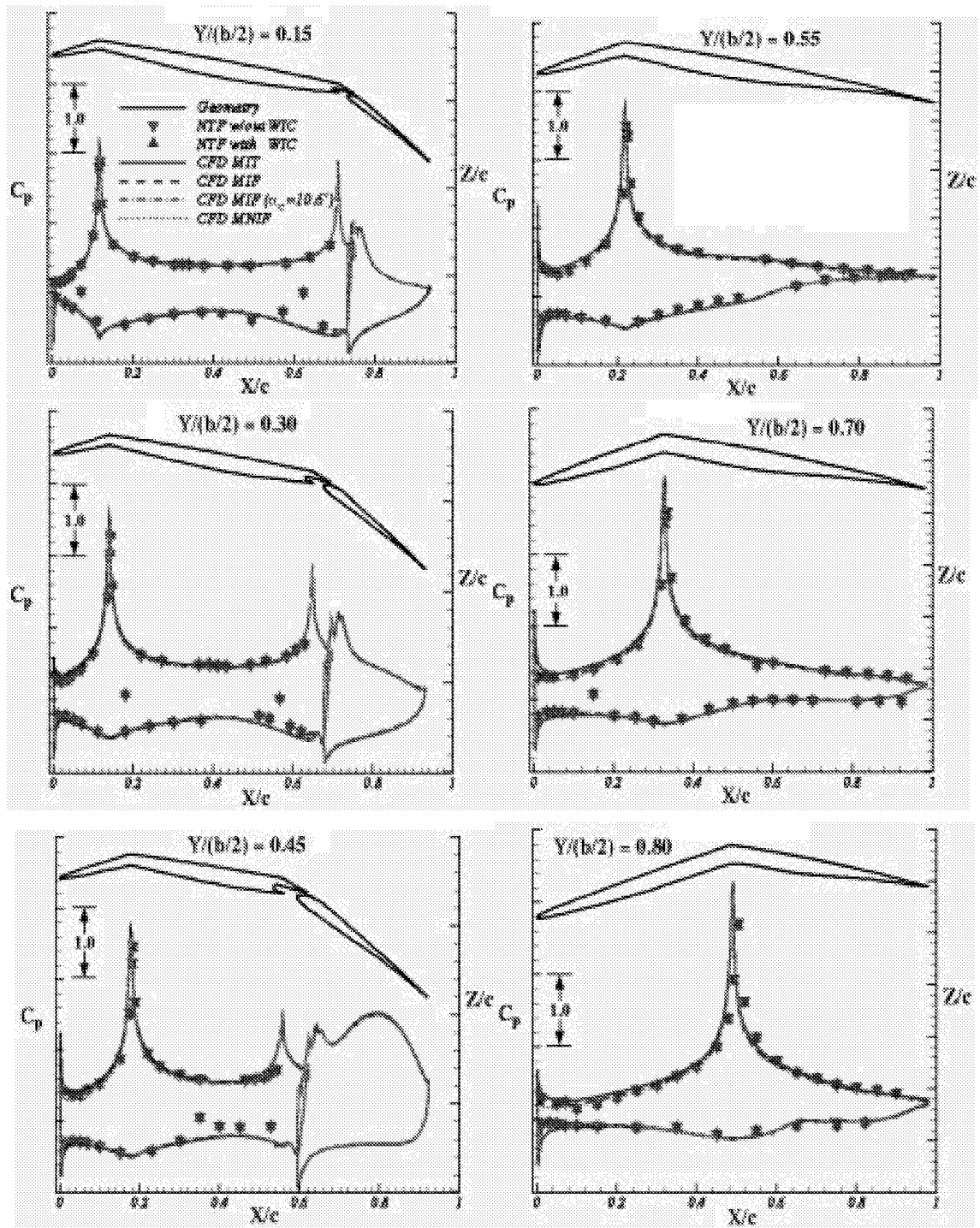


(a) Overall view of the solution.



(b) Close up view of the model.

Figure 17. Turbulent Navier-Stokes flow field simulation for the semispan model in free air.



(a) Inboard high-lift stations.

(b) Outboard wing stations.

Figure 18. Computed wing surface pressure coefficients and correlation with data.

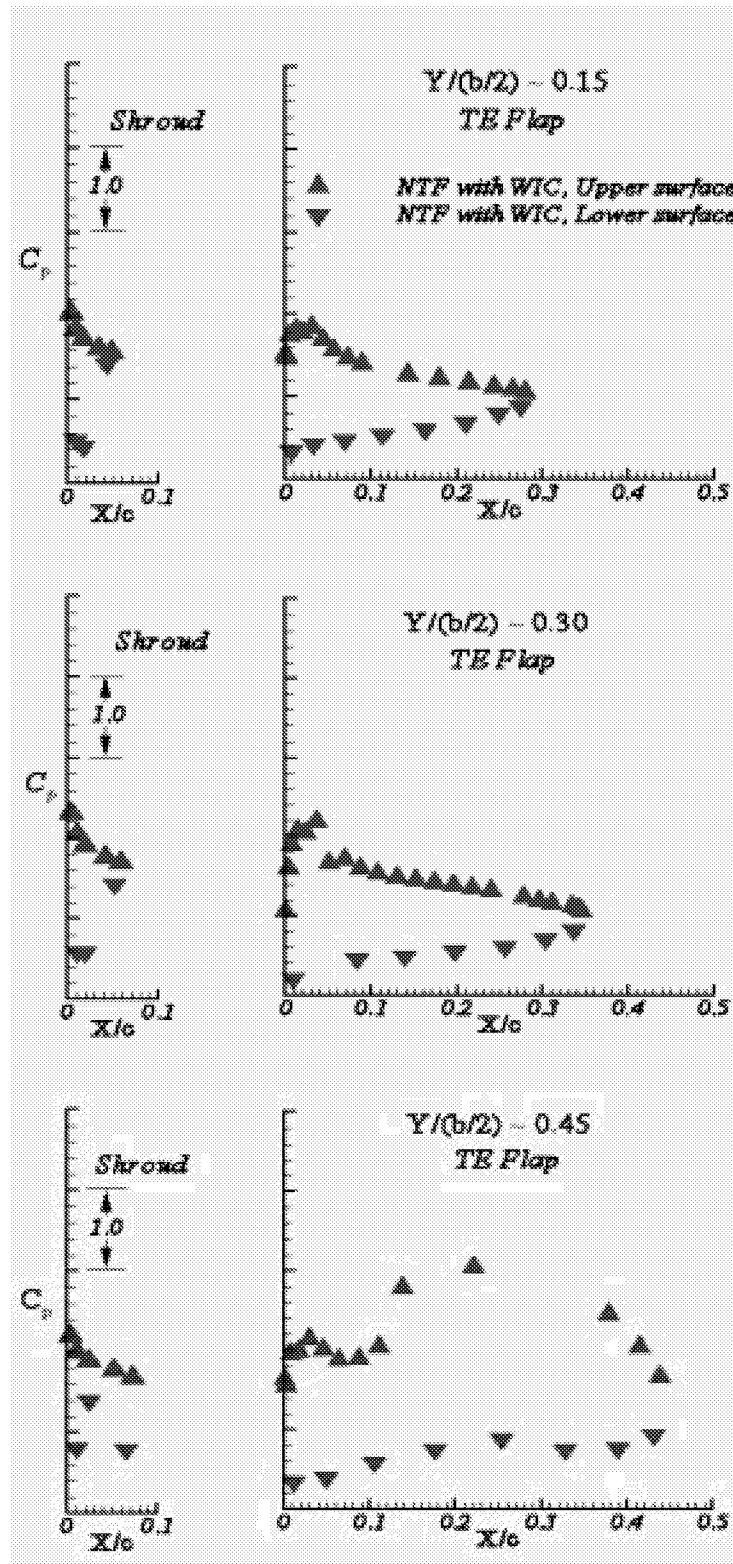


Figure 19. Experimental surface pressure coefficients over the shroud and TEF.

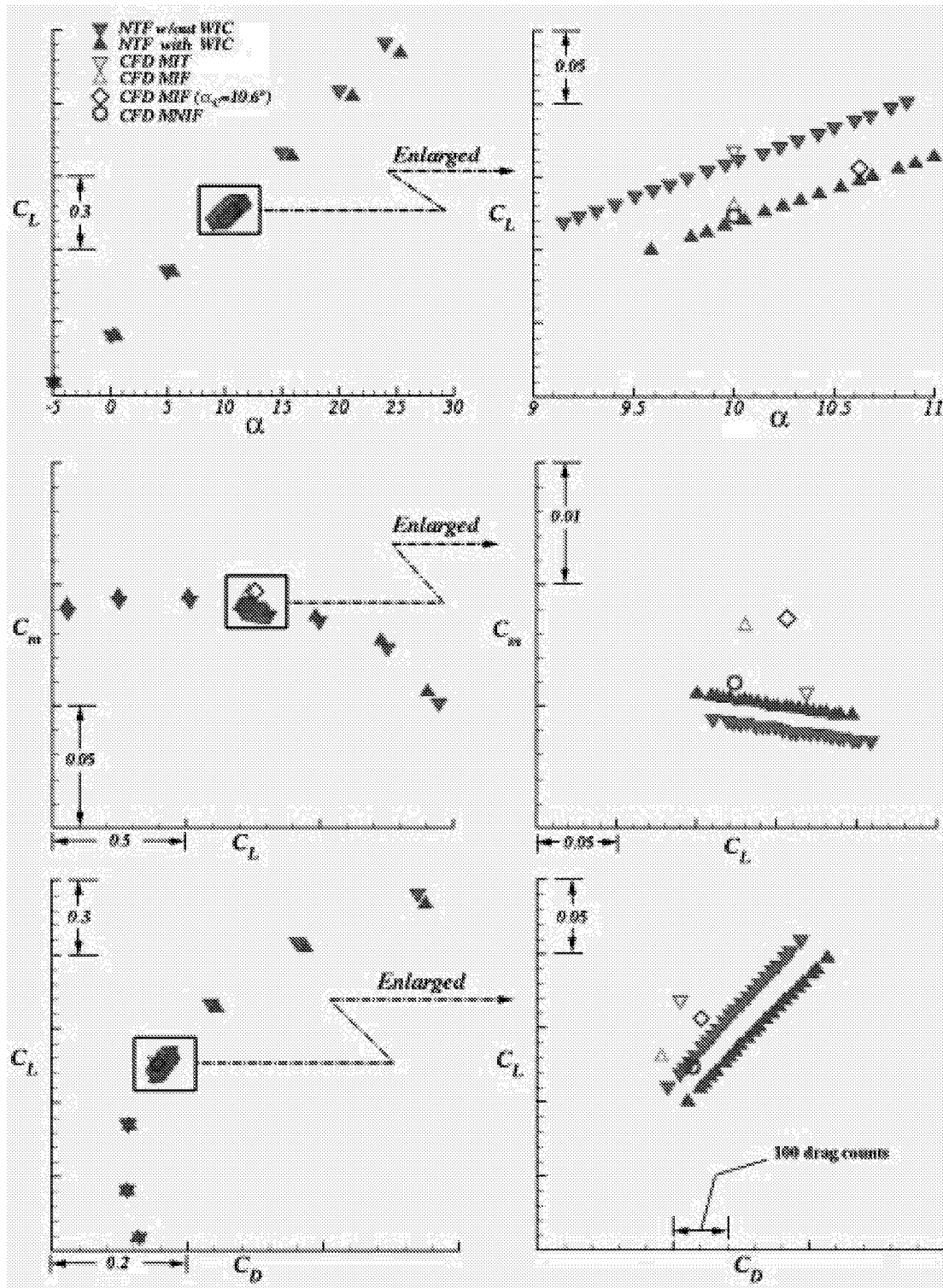


Figure 20. Computed and measured longitudinal aerodynamic characteristics.

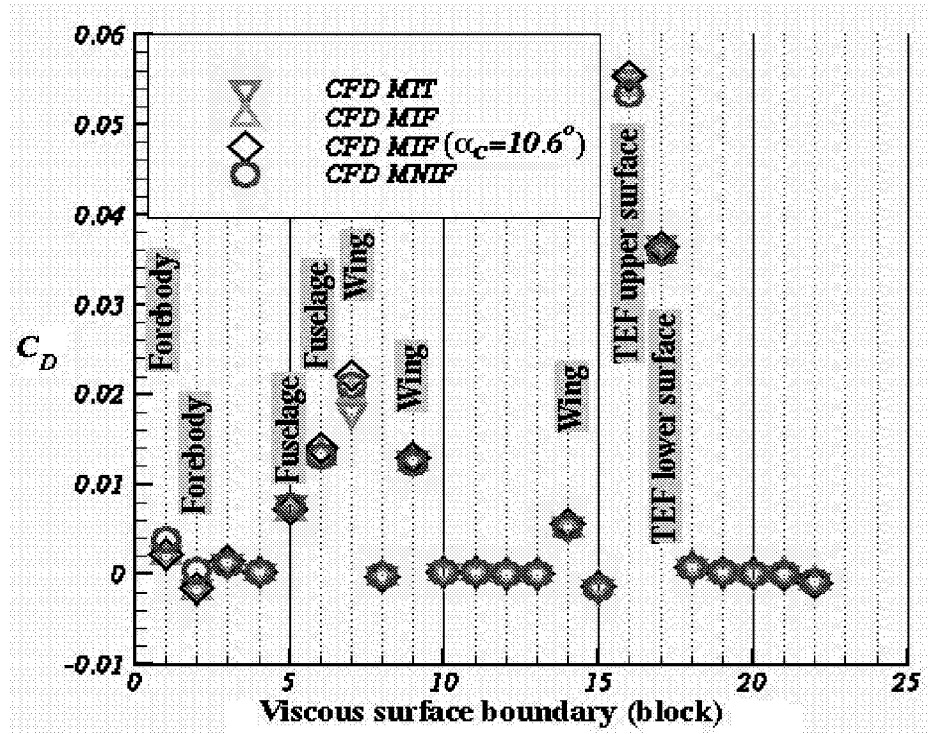


Figure 21. Computed drag coefficients for configuration various components (blocks).

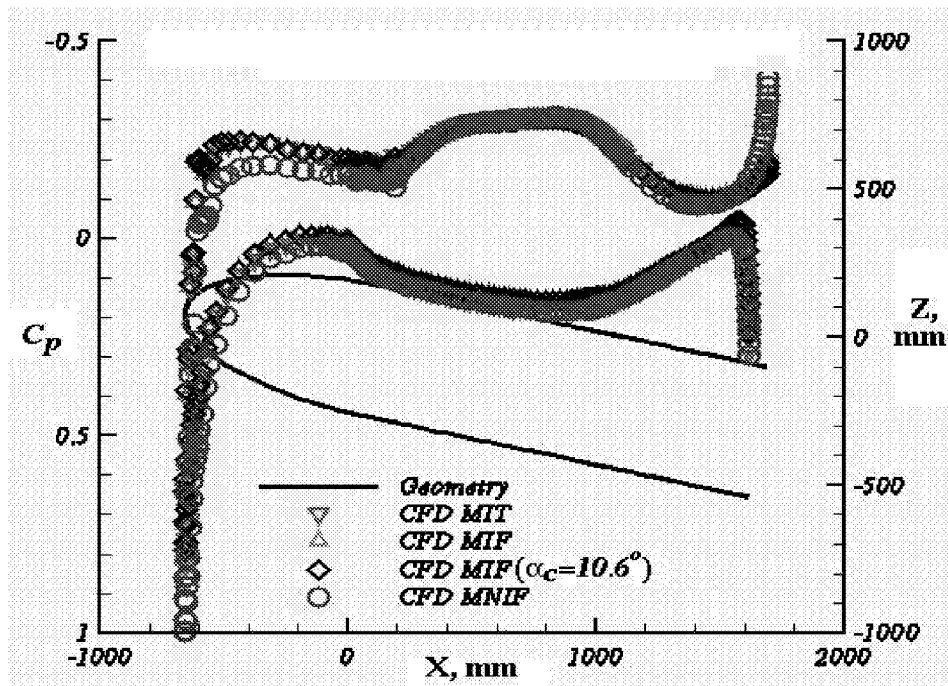


Figure 22. Computed longitudinal C_p along the fuselage centerline, $Y=0$ mm.

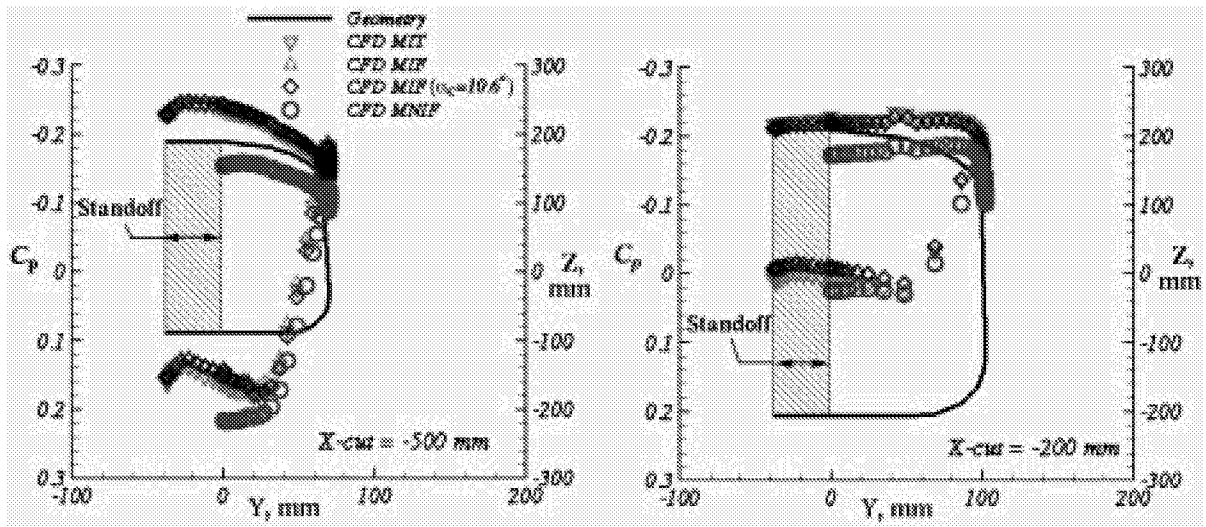
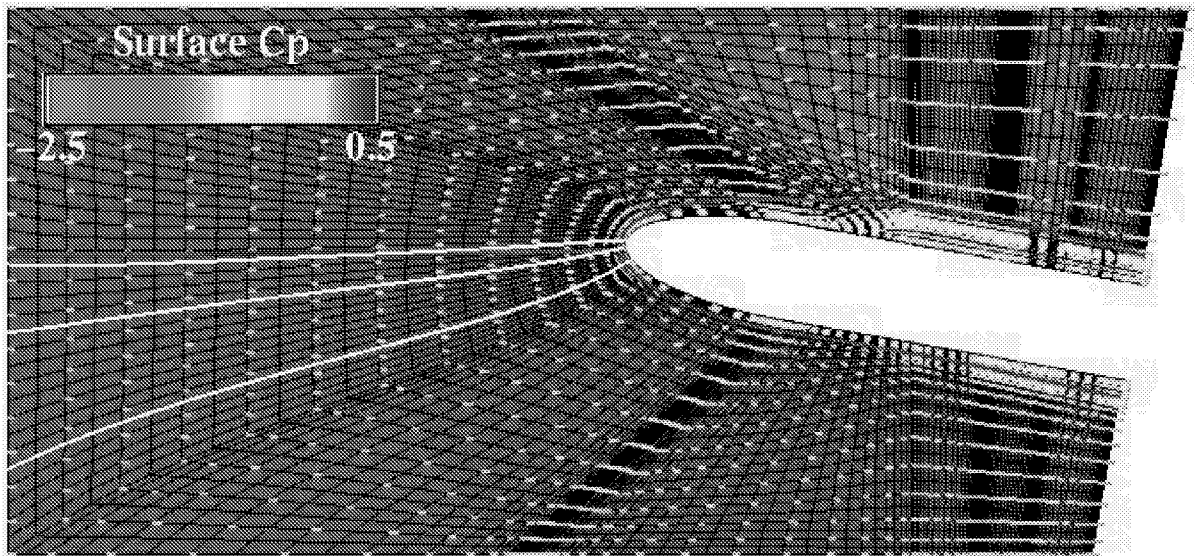
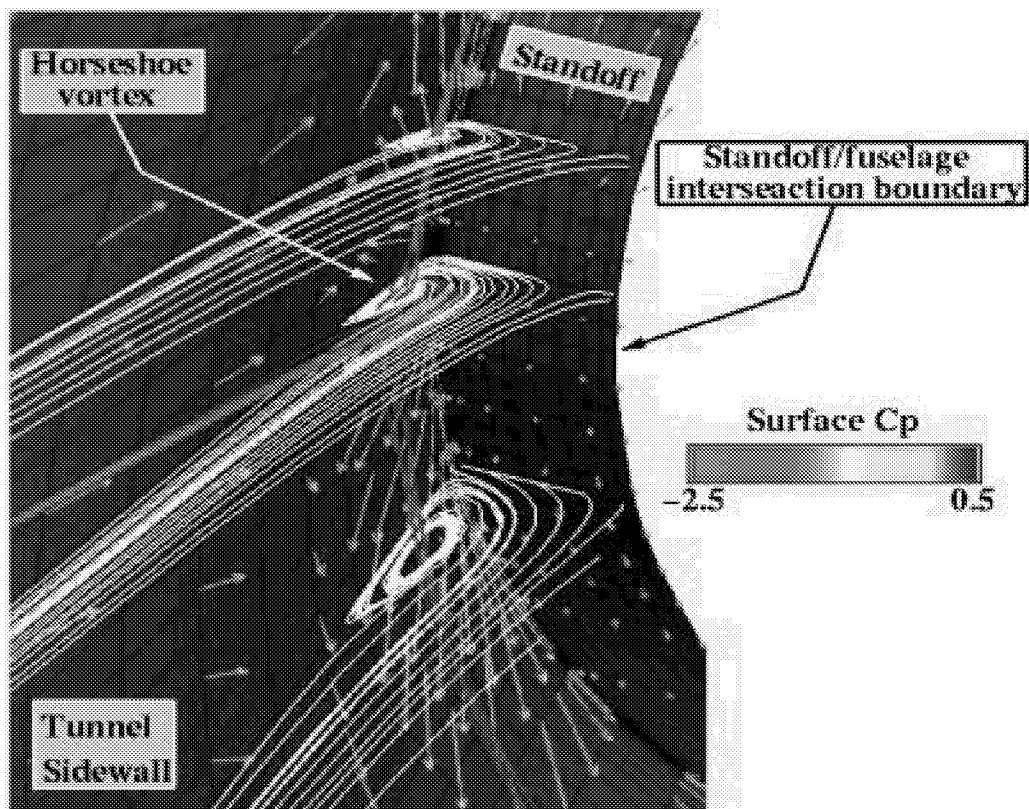


Figure 23. Computed circumferential pressure distributions at two forebody stations.



(a) Side view.

Figure 24. Computed total velocity vectors on the tunnel sidewall, standoff (second grid off the surface) and off-surface particle traces (only a portion of the grid shown).



(b) Oblique close-up view of the tunnel sidewall horseshoe vortex structure ahead of the standoff.

Figure 24. Concluded.

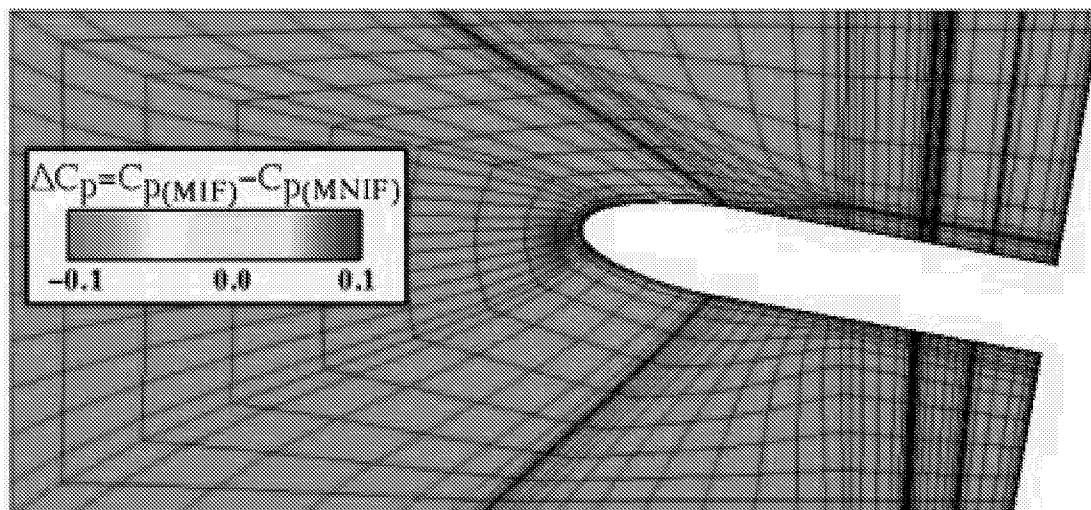


Figure 25. Computed pressure coefficient difference between MIF and MNIF in plane-of-symmetry (only a portion of the grid is shown).

REPORT DOCUMENTATION PAGE			Form Approved OMB No. 0704-0188	
Public reporting burden for this collection of information is estimated to average 1 hour per response, including the time for reviewing instructions, searching existing data sources, gathering and maintaining the data needed, and completing and reviewing the collection of information. Send comments regarding this burden estimate or any other aspect of this collection of information, including suggestions for reducing this burden, to Washington Headquarters Services, Directorate for Information Operations and Reports, 1215 Jefferson Davis Highway, Suite 1204, Arlington, VA 22202-4302, and to the Office of Management and Budget, Paperwork Reduction Project (0704-0188), Washington, DC 20503.				
1. AGENCY USE ONLY (Leave blank)		2. REPORT DATE August 2002		3. REPORT TYPE AND DATES COVERED Technical Publication
4. TITLE AND SUBTITLE Turbulent Navier-Stokes Flow Analysis of an Advanced Semispan Diamond-Wing Model in Tunnel and Free Air at High-Lift Conditions			5. FUNDING NUMBERS 522-31-31-06	
6. AUTHOR(S) Farhad Ghaffari, Robert T. Biedron, and James M. Luckring				
7. PERFORMING ORGANIZATION NAME(S) AND ADDRESS(ES) NASA Langley Research Center Hampton, VA 23681-2199			8. PERFORMING ORGANIZATION REPORT NUMBER L-18111	
9. SPONSORING/MONITORING AGENCY NAME(S) AND ADDRESS(ES) National Aeronautics and Space Administration Washington, DC 20546-0001			10. SPONSORING/MONITORING AGENCY REPORT NUMBER NASA/TP-2002-211779	
11. SUPPLEMENTARY NOTES Available electronically at the following URL address: http://techreports.larc.nasa.gov/ltrs				
12a. DISTRIBUTION/AVAILABILITY STATEMENT Unclassified-Unlimited Subject Category 02 Distribution: Standard Availability: NASA CASI (301) 621-0390			12b. DISTRIBUTION CODE	
13. ABSTRACT (Maximum 200 words) Turbulent Navier-Stokes computational results are presented for an advanced diamond wing semispan model at low-speed, high-lift conditions. The numerical results are obtained in support of a wind-tunnel test that was conducted in the National Transonic Facility at the NASA Langley Research Center. The model incorporated a generic fuselage and was mounted on the tunnel sidewall using a constant-width non-metric standoff. The computations were performed at a nominal approach and landing flow conditions. The computed high-lift flow characteristics for the model in both the tunnel and in free-air environment are presented. The computed wing pressure distributions agreed well with the measured data and they both indicated a small effect due to the tunnel wall interference effects. However, the wall interference effects were found to be relatively more pronounced in the measured and the computed lift, drag and pitching moment. Although the magnitudes of the computed forces and moment were slightly off compared to the measured data, the increments due the wall interference effects were predicted reasonably well. The numerical results are also presented on the combined effects of the tunnel sidewall boundary layer and the standoff geometry on the fuselage forebody pressure distributions and the resulting impact on the configuration longitudinal aerodynamic characteristics.				
14. SUBJECT TERMS Computational fluid dynamics, Multiblock structured grid, Turbulent viscous flow, Spalart-Allmaras, High-lift aerodynamics, Tunnel wall effects, Semispan model			15. NUMBER OF PAGES 39	
			16. PRICE CODE	
17. SECURITY CLASSIFICATION OF REPORT Unclassified	18. SECURITY CLASSIFICATION OF THIS PAGE Unclassified	19. SECURITY CLASSIFICATION OF ABSTRACT Unclassified	20. LIMITATION OF ABSTRACT UL	